Mon. Not. R. Astron. Soc. **000**, 1–20 (2008) Printed 21 June 2012 (MN LATEX style file v2.2)

Relaxation and Stripping: The Evolution of Sizes, Dispersions and Dark Matter Fractions in Major and Minor Mergers of Elliptical Galaxies

Michael Hilz[1,2],Thorsten Naab[1⋆],Jeremiah P. Ostriker[3],Jens Thomas[4], Andreas Burkert[2] and Roland Jesseit[5]
[1] *Max-Planck-Institut für Astrophysik, Karl-Schwarzschild-Str. 1, 85741 Garching, Germany*
[2] *Universitäts-Sternwarte München, Scheinerstr. 1 ,D-81679 München, Germany*
[3] *Department of Astrophysical Sciences, Princeton University, Princeton, NJ 08544, USA*
[4] *Max-Planck-Institut für extraterrestrische Physik, Giessenbachstrasse, D-85748 Garching, Germany*
[5] *Lifeware SA, Asylstrasse 112,CH-8032 Zürich, Switzerland*

Accepted ???. Received ??? in original form ???

ABSTRACT
We revisit collisionless major and minor mergers of spheroidal galaxies in the context of recent observational insights on compact massive early-type galaxies at high redshift and their rapid evolution on cosmological timescales. The simulations are performed as a series of mergers with mass-ratios of 1:1 and 1:10 for models representing pure bulges as well as bulges embedded in dark matter halos. For major and minor mergers, respectively, we identify and analyze two different processes, violent relaxation and stripping, leading to size evolution and a change of the dark matter fraction within the observable effective radius $r_{\rm e}$. Violent relaxation - which is the dominant mixing process for major mergers but less important for minor mergers - scatters relatively more dark matter particles than bulge particles to radii $r < r_{\rm e}$. Stripping in minor mergers assembles stellar satellite particles at large radii in halo dominated regions of the massive host. This strongly increases the size of the bulge into regions with higher dark matter fractions leaving the inner host structure almost unchanged. A factor of two mass increase by minor mergers increases the dark matter fraction within the effective radius by 80 per cent whereas relaxation in one equal-mass merger only leads to an increase of 25 percent. We present analytic corrections to simple one-component virial estimates for the evolution of the gravitational radii. These estimates are shown to underpredict the evolution of the effective radii for parabolic minor mergers of bulges embedded in massive dark matter halos. If such a two-component system grows by minor mergers alone its size growth, $r_{\rm e} \propto M^{\alpha}$, reaches values of $\alpha \approx 2.4$, significantly exceeding the simple theoretical limit of $\alpha = 2$. For major mergers the sizes grow with $\alpha \lesssim 1$. In addition, we discuss the velocity dispersion evolution and velocity anisotropy profiles. Our results indicate that minor mergers of galaxies embedded in massive dark matter halos provide a potential mechanism for explaining the rapid size growth and the build-up of massive elliptical systems predicting significant dark matter fractions and radially biased velocity dispersions at large radii.

Key words: galaxies: ellipticals - galaxies: evolution - galaxies: dynamics - galaxies: structure - methods: N-body simulations

1 INTRODUCTION

Recent observations have revealed a population of very compact, massive ($\approx 10^{11} M_{\odot}$) and quiescent galaxies at z∼2 with sizes of about ≈ 1kpc (Daddi et al. 2005; Trujillo et al. 2006; Longhetti et al. 2007; Toft et al. 2007; Zirm et al. 2007; Trujillo et al. 2007; Zirm et al. 2007; Buitrago et al. 2008; van Dokkum et al. 2008; Cimatti et al. 2008; Franx et al. 2008; Saracco et al. 2009; Damjanov et al. 2009; Bezanson et al. 2009; Newman et al. 2010; Szomoru et al. 2012; McLure et al. 2012). Elliptical galaxies of a similar mass today are larger by a factor

⋆ E-mail: naab@mpa-garching.mpg.de

of 4 - 5 (van der Wel et al. 2008) with at least an order of magnitude lower effective densities and significantly lower velocity dispersions than their high-redshift counterparts (van der Wel et al. 2005, 2008; Cappellari et al. 2009; Cenarro & Trujillo 2009; van Dokkum et al. 2009; van de Sande et al. 2011a; Szomoru et al. 2011; Martinez-Manso et al. 2011). The measured small effective radii are most likely not caused by observational limitations, although the low density material in the outer parts of distant galaxies is difficult to detect (Hopkins et al. 2009). Their clustering, number densities and core properties indicate that they are probably the progenitors of the most massive ellipticals and Brightest Cluster Galaxies today (Hopkins et al. 2009; Bezanson et al. 2009). Such compact massive galaxies are extremely rare in the nearby universe (Trujillo et al. 2009; Taylor et al. 2010, see also Valentinuzzi et al. 2010; Raichoor et al. 2012; Jiang et al. 2012; Ferré-Mateu et al. 2012; Trujillo et al. 2012).

The high phase-space densities of these compact $z = 2 - 3$ systems imply a formation mechanism that is dominated by dissipational processes (Kereš et al. 2005; Naab et al. 2007, 2009; Joung et al. 2009; Dekel et al. 2009; Kereš et al. 2009; Johansson et al. 2009; Oser et al. 2010; Wuyts et al. 2010; Bournaud et al. 2011; Oser et al. 2012; Johansson et al. 2012). Frequent stellar minor and major mergers, as also expected in a cosmological context, are promising physical mechanism to explain the subsequent rapid size growth in the absence of significant additional dissipation and star formation (Cole et al. 2000; Khochfar & Silk 2006; De Lucia et al. 2006; Guo & White 2008; Bezanson et al. 2009; Hopkins et al. 2010; Trujillo et al. 2011; Cooper et al. 2012; McLure et al. 2012).

Observations and theoretical studies provide evidence that massive early-type galaxies undergo on average about one major merger since redshift ~ 2 but significantly more minor mergers per unit time (Bell et al. 2006; Khochfar & Silk 2006; Bell et al. 2006; Genel et al. 2008; Lotz et al. 2011). However, merger rates are notoriously difficult to measure and the uncertainties are still large, but assuming a canonical value of one major merger since $z = 2$, this would not be sufficient to explain the observed size evolution (Bezanson et al. 2009; Trujillo et al. 2011; Williams et al. 2011). In addition, major mergers are highly stochastic and some massive galaxies should have experienced no major merger at all, and would therefore still be compact today. Direct numerical simulations in a full cosmological context support the importance of numerous minor mergers for the assembly of massive galaxies whose dissipative formation phase is followed by a second phase dominated by stellar accretion (predominantly minor mergers) onto the galaxy, driving the size evolution (Khochfar & Silk 2006; Naab et al. 2009; Oser et al. 2010; Lackner & Gunn 2012). This theoretical finding is supported by recent direct observational and circumstantial evidence that has recently been presented in support of minor mergers (van Dokkum et al. 2010; Trujillo et al. 2011; Williams et al. 2011; Cooper et al. 2012).

Minor mergers are particularly efficient in reducing the effective stellar densities, mildly reducing the velocity dispersions, and rapidly increasing the sizes, building up extended stellar envelopes (Miller & Smith 1980; Villumsen 1983; Farouki et al. 1983; Naab et al. 2009; Bournaud et al. 2007; Bezanson et al. 2009; Hopkins et al. 2010; Oser et al. 2010, 2012; Laporte et al. 2012; Lackner & Ostriker 2010). However, there are some doubts as to whether minor mergers alone are sufficient or whether additional physical processes are required (Naab et al. 2006; Nipoti et al. 2009, 2012; Newman et al. 2012; Cimatti et al. 2012). Major mergers of ellipticals will contribute to mass growth and will change kinematic properties (Naab et al. 2006). However, their impact on the evolution of stellar densities, velocity dispersions and sizes is relatively weak (White 1978, 1979; Boylan-Kolchin et al. 2005; Nipoti et al. 2009).

Using the virial theorem, Cole et al. (2000), Naab et al. (2009) and Bezanson et al. (2009) presented a simple analytical estimate of how sizes, densities and velocity dispersions of one-component collisionless systems evolve during parabolic, purely stellar mergers with different mass ratios. According to this simplified model, the accretion of loosely bound material (minor mergers) results in a significantly stronger size increase than predicted for major mergers (Naab et al. 2009). Using a similar approach Bezanson et al. (2009) argued that eight successive mergers of mass ratio 1:10 can lead to a size increase of ~ 5, which corresponds to the observed difference between old compact galaxies and massive ellipticals today. Of course, this is only valid for global system properties like the gravitational radii and total mean square speeds. The simple virial estimates presented by Naab et al. (2009); Bezanson et al. (2009) did not include violent relaxation effects like mass loss, occurring during the encounter or non-homology. However, Ciotti et al. (2007) presented a more general study including the effect of gas dissipation and non-homology.

Early papers on the interactions of spheroidal galaxies already discussed many of the aforementioned effects using N-body simulations of one-component spherical systems. White (1978, 1979), who made one of the first simulations of this kind, already found that relaxation effects are important in equal-mass encounters and change the internal structure of the remnants. The central regions contract and diffuse envelopes build up (see also Miller & Smith 1980; Villumsen 1983; Farouki et al. 1983), leading to a break in homology. Furthermore, equal-mass mergers lead to the redistribution of particles eventually reducing population gradients (White 1980; Villumsen 1983). This is different in unequal-mass mergers, which can enhance population gradients by depositing satellite stars at large radii (Villumsen 1983). However, these early models did not investigate the influence of an extended and massive dark matter halo.

Although dissipationless minor mergers theoretically lead to an increase in sizes and a decrease of velocity dispersions, it is not clear whether this scenario works quantitatively. Nipoti et al. (2003), using two-component models - argued that dry major and minor mergers alone cannot be the main mechanism governing the late evolution of elliptical galaxies, because their simulated merger remnants did not follow the Faber-Jackson (Faber & Jackson 1976) and Kormendy relations (Kormendy 1977), although they stayed on the fundamental plane. Still, dry major and minor mergers can bring compact early-type galaxies closer to the fundamental plane but the size increase estimated from idealized models taking into account the cosmological context might be too weak (Nipoti et al. 2009, 2012; Cimatti et al. 2012).

In this paper we revisit collisionless one- and two-component equal-mass and minor mergers focusing on the merger dynamics and the effect of a dark matter halo on the resulting evolution of global theoretical and observable galaxy properties. In section 2 we present the method used to construct equilibrium one- and two-component systems. The effects of violent relaxation and stripping are discussed in section 3 followed by a detailed discussion of analytic estimates for the structural evolution based on the virial theorem in section 4. In section 5 we present the evolution of observable galaxy properties. We summarize and discuss the results in section 6.

2 NUMERICAL METHODS

2.1 Galaxy models

For the initial galaxy models we assume spherical symmetric, isotropic Hernquist density profiles (Hernquist 1990) for the luminous as well as the dark matter component,

$$\rho_i(r) = \frac{M_i}{2\pi}\frac{a_i}{r(r+a_i)^3}, \tag{1}$$

where ρ_i, M_i and a_i are the density, the mass and the scale length of the respective component i. The potential is

$$\Phi_i(r) = -\frac{GM_i}{r+a_i}, \tag{2}$$

with the gravitational constant G.

On the one hand the projected Hernquist profile is a reasonable approximation of the $R^{1/4}$ law (de Vaucouleurs 1948) for the luminous component (its Sersic index however is closer to $n \sim 2.6$, see Naab & Trujillo 2006). On the other hand it is a good representation of the Navarro et al. (1997) profile for the dark matter component. Therefore we consider the Hernquist density distribution a sufficiently realistic description for the luminous and dark matter distributions of a typical elliptical galaxy.

For simplicity, we assume isotropy of the velocity distribution to construct a stable initial configuration, and the bulge and halo component are in dynamical equilibrium. We compute the distribution function (DF) f_i for each component i, using Eddington's formula (Binney & Tremaine 2008),

$$f_i(E) = \frac{1}{\sqrt{8}\pi^2}\int_{\Phi=0}^{\Phi=E}\frac{d^2\rho_i}{d\Phi_T^2}\frac{d\Phi_T}{\sqrt{E-\Phi_T}}, \tag{3}$$

where ρ_i is the density profile of component i, E is the relative (positive) energy and Φ_T is the total gravitational potential $\Phi_T = \Phi_*(+\Phi_{dm})$. Solving distribution functions, is in general more complicated than using Jeans equations, but results in more stable initial conditions (Kazantzidis et al. 2004). The distribution function of a two component Hernquist model can be computed analytically, even in the anisotropic case (Ciotti 1996). Our model, however, also allows for more general density distributions and we calculate f_i numerically. As in our approach we have no analytic expression for $\rho_i(\Phi_T)$ (see Eq. 3) we have to transform the integrand of Eq. 3 to be a function of radius r,

$$\frac{d^2\rho_i}{d\Phi_T^2}d\Phi_T = \left(\frac{d\Phi_T}{dr}\right)^{-2}\left[\frac{d^2\rho_i}{dr^2} - \left(\frac{d\Phi_T}{dr}\right)^{-1}\frac{d^2\Phi_T}{dr^2}\frac{d\rho_i}{dr}\right]\frac{d\Phi_T}{dr}dr. \tag{4}$$

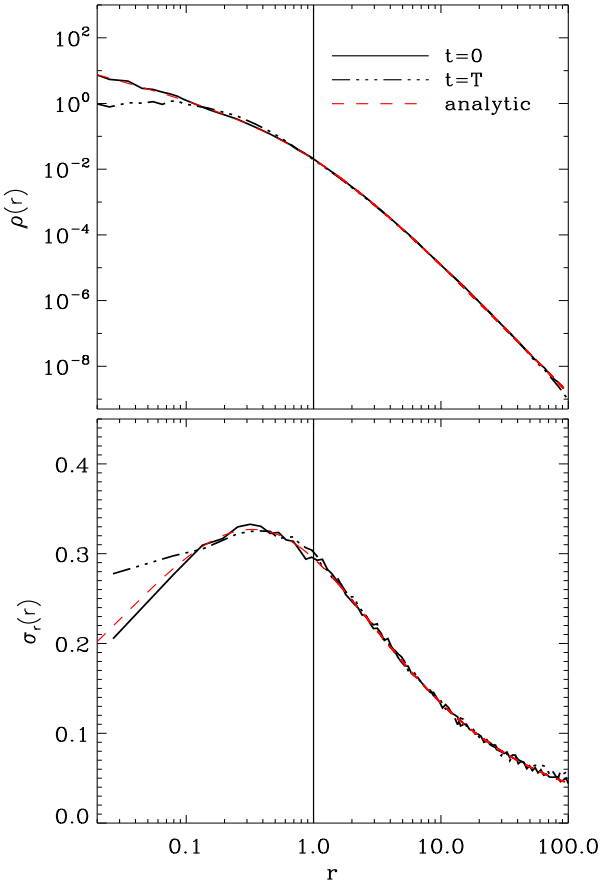

Figure 1. Top panel: Radial density profile for a Hernquist distribution (160k particles). The black solid line illustrates the initial profile (t=0) and the dashed-dotted line the final profile ($t = T \sim 100 \times t_{dyn}$, where t_{dyn} is the dynamical time at the spherical half-mass radius).The analytical profile is indicated by the red dashed line. Inside 10% of the scale length (vertical solid line) the system is affected (increase in dispersion and decrease in density) by two-body effects. They conduct heat into the initially cooler central regions. However, overall, the system is dynamically stable for at least 100 dynamical times. Bottom panel: Initial (solid line) and final (black dashed line) radial velocity dispersion profile.

This procedure always results in an analytical expression for the integrand, even for more general γ- profiles (Dehnen 1993) with different slopes for the density distribution. As a consequence, the integration limits also have to change, e.g. $\Phi(r) = 0$ gets $r = \infty$ and $\Phi(r) = E$ has to be solved (numerically) for the radius r.

Once we have computed the DF we can randomly sample particles with radii smaller than a given cut-off radius and random velocities, which are smaller than the escape velocity. Then the particle configuration for the galaxy is established using the Neumann rejection method.

The one component model is described by two parameters, the scale length a_* and the total mass M_*. For the two component models, including dark matter, we additionally

introduce the dimensionless parameters μ and β for the scale length of the halo $a_{dm} = \beta a_*$ and its mass $M_{dm} = \mu M_*$.

2.2 Model Parameters and Merger Orbits

For the total dark matter to stellar mass ratio we assume $\mu = M_{dm}/M_* = 10$ and the ratio of the scale radii is $\beta = a_{dm}/a_* = 11$, for all simulations with two-component models. We perform a set of simulations for two different scenarios; both adopt $M_* = a_* = 1.0$. In the major merger scenario we simulate mergers of initially identical, spherically symmetric one- or two-component models on zero energy orbits. The encounters have parabolic orbits with and without angular momentum (head-on). For higher merger generations we duplicate the merger remnant after reaching dynamical equilibrium at the center and merge them again on orbits with the same energy but different infall directions. In total, we simulate three generations of head-on equal-mass mergers, and two generations with angular momentum (see also Table 1).

In the minor merger scenario our simulation sequences start with an initial mass ratio of 1:10, i.e. $M_{\rm host} = 10 M_{\rm sat}$ and a stellar scale radius of the satellite of $a_{*,\rm sat} = 1.0$. This choice for the satellite's scale radius seems unrealistically large but there are no direct observations for low mass galaxies at high redshift and the sizes of less massive ellipticals at present converge towards an effective radius of $r_e \sim 1kpc$ (Misgeld & Hilker 2011). Therefore the satellite galaxies have the same size as the compact early-type hosts, although they are an order of magnitude less massive. For comparison, we simulated two sequences (with one- and two-component models), of head-on minor mergers, where the satellite's scale radii are half the host's scale radius $a_{*,\rm sat} = 0.5$, though the satellites lie on an extrapolation of the observed mass-size relation of Williams et al. (2010) at $z = 2$ (see Table 1). The host galaxy for the next generation is the virialized end product of the previous accretion event. This host is merged with a satellite identical to the first generation. The mass ratio for this merger is now 1:11. We repeat this procedure until the host galaxy has doubled its mass, i.e. 10 minor mergers. The final mass ratio of the merger is 1:19. Again we simulate one- and two-component mergers with zero (head-on) and non-zero angular momentum. As the mergers of the bulge+halo model with angular momentum are computationally expensive we only simulate 6 generations.

For all head-on mergers we separate the centers by a distance d and assign them a relative velocity $v_{\rm rel} = 2\sqrt{GM_h/d}$, where M_h is the total attracting mass of the host galaxy within the radius d. This velocity corresponds to an orbit with zero energy and zero angular momentum, i.e. the galaxies will have a zero relative velocity at infinite distance. The distance d is always large enough to obtain virialized remnants at the end of each generation. As the merger remnants after the first generation will not be spherical anymore, their mutual orientation is randomly assigned at the beginning of each new merger event. For the mergers with angular momentum we set the impact parameters to half of the spherical half-mass radius of the host's bulge and separate the galaxies for enough so that the initial overlap is very small.

Run	Gen.	$a_{*,sat}$	$M_{ub}(\%)$	$M_{*,ub}(\%)$
B1ho	3	1.0	12.3	12.3
B1am	2	1.0	15.0	15.0
HB1ho	3	1.0	10.1	2.5
HB1am	2	1.0	8.8	2.0
B10hod	10	1.0	21.8	21.8
B10amd	10	1.0	20.9	20.9
B10hoc	10	0.5	21.7	21.7
HB10hod	10	1.0	35.6	20.4
HB10amd	6	1.0	19.5	7.9
HB10hoc	10	0.5	20.9	7.2

Table 1. This table gives the name of the hierarchy (1st column), the number of generations (2nd), the initial scale radius of the satellite (3rd), the amount of unbound mass of the total final remnant (4th) and the corresponding stellar mass loss (5th). The name can be explained as followed; B/HB: bulge or bulge+halo, 1/10: major/minor merger, am/ho: orbit with/without angular momentum. In the case of the minor merger scenarios, c/d indicates wether we chose a compact or diffuse satellite.

2.3 Simulations and Stability Tests

All simulations were performed with VINE (Wetzstein et al. 2009; Nelson et al. 2009), an efficient, parallelized tree-code. We use a spline softening kernel with a softening length $\epsilon = 0.02$ for all runs. In general, the softening length depends on the particle number (e.g. Merritt 1996;Dehnen 2001) and we found $\epsilon = 0.02$ to result in stable models. For the major merger simulations the host galaxy consists of $N_* = 1.6\times10^5$ bulge particles for the one-component (bulge only) model and $N_* = 2\times10^4$ for the two-component model, which has an additional halo represented by $N_{\rm DM} = 2\times10^5$ particles of the same mass. For the accretion scenario, the one- and two-component host galaxies both have $N_* = 10^5$ bulge particles and the latter has $N_{\rm DM} = 10^6$ halo particles. The satellites have ten times fewer particles for all components.

In Fig. 1 we demonstrate the stability of the bulge only model with 160k particles by comparing the initial and final (100 dynamical times) density (top panel) and radial velocity dispersion (bottom panel) as a function of radius to the analytical values. In general the model is very stable for the full simulation time, except in the innermost parts, where two-body relaxation becomes important. At the highest densities, inside 10% of the scale radius the relaxation time $t_{\rm relax}$ of the model is very small ($t_{\rm relax} \sim 50 \cdot t_{\rm dyn}$). Consequently, two-body encounters change the central particle's energy and deplete the high density regions. Looking at the initial and final number of particles within $0.1a_*$, we find that half of the particles escape this region and go to lower binding energies. However, at larger radii the models are very stable with a very good agreement to the analytical solution. The radii enclosing 30, 50 and 80 per cent of the stellar mass stay perfectly constant.

The stability of the two-component system is demonstrated in Fig. 2. Our initial model, constructed of two Hernquist spheres, is again very stable over a long simulation period of more than 60 dynamical times (Figure 2). The density and the velocity dispersion do not change significantly. Again the innermost regions are affected by two-body relaxation. However, looking at the mass radii of the bulge and the halo we observe no big changes. The apparent contrac-

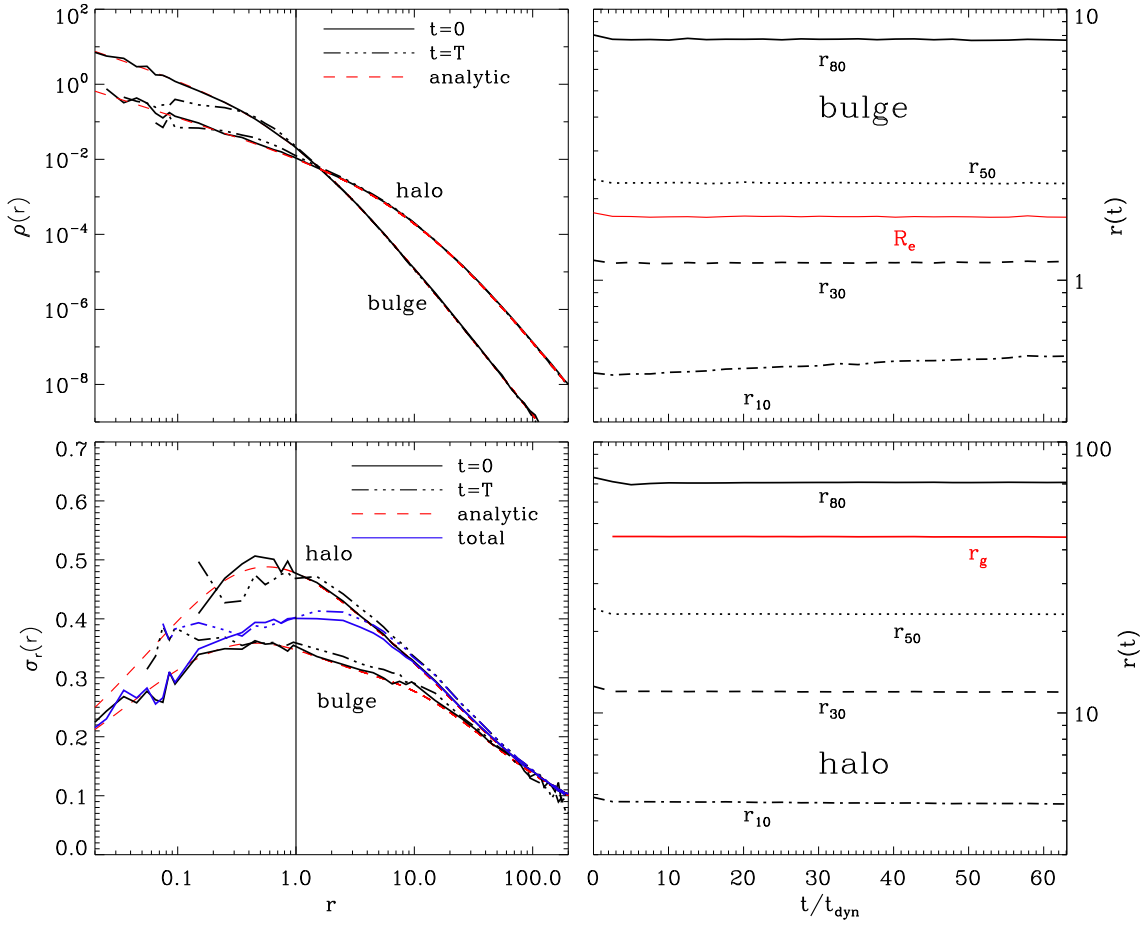

Figure 2. Top left panel: Radial density profile for the two-component realization with 1100k particles. The bulge to halo mass ratio is 1:10. The solid black lines illustrate the initial profiles (t=0) of the bulge and the halo and the dashed-dotted lines their final profiles ($t > 60t_{dyn}$). The analytic Hernquist profiles are indicated by the red dashed line. Bottom left panel: Radial velocity dispersion of the total system (blue solid: initially, blue dashed-dotted: final), the bulge and the halo separately. Inside $0.3a_*$ the model is affected by two-body relaxation, but overall it is stable. Right panels: Time evolution of the radii enclosing 80%, 50%, 30% and 10% mass (black lines from top to bottom) of the bulge (top panel) and halo (bottom panel). The red lines show the effective radius of the bulge (upper panel) and the gravitational radius of the whole system (bottom panel). Except for the 10% radius of the bulge, which shows a slight increase, all mass radii stay constant over > 60 dynamical times.

tion of the mass radii enclosing 80% or 50% is less than 5% for the halo and less than 2% for the bulge. The gravitational radius and the effective radius which we use in this paper stay constant. Therefore we conclude that the regions we are interested in are not affected by two-body relaxation and other numerical effects of the initial conditions, and the results of our merger simulations should be robust for our choice of force resolution and particle numbers.

3 RELAXATION & STRIPPING

Our set of simulations indicate that dissipationless mergers of spheroids are strongly affected by two dynamical processes, *violent relaxation* which dominates the evolution of major mergers and *tidal stripping* which is important for minor mergers. In the following we will discuss both processes in more detail.

3.1 Major Mergers

For equal-mass mergers, the effect of violent relaxation is very strong and has a significant effect on the differential energy distribution of the remnants. The left panel of Fig. 3 indicates, that the initial narrow distribution (black line) becomes broader with each generation. Tightly bound particles become even more bound and some weakly bound particles gain enough energy to escape the galactic potential. The theoretical framework of violent relaxation is very complex and, since the pioneering work of Lynden-Bell (1967), there have been many approaches to obtain a viable theory, which can describe the final equilibrium configuration of a violently relaxing system (e.g. Shu 1978; Nakamura 2000; Arad & Johansson 2005). In the following we first give a short introduction to the original approach of Lynden-Bell (1967), before we discuss our results with respect to another slightly different approach of Spergel & Hernquist (1992).

During the approach and interaction of two collision-

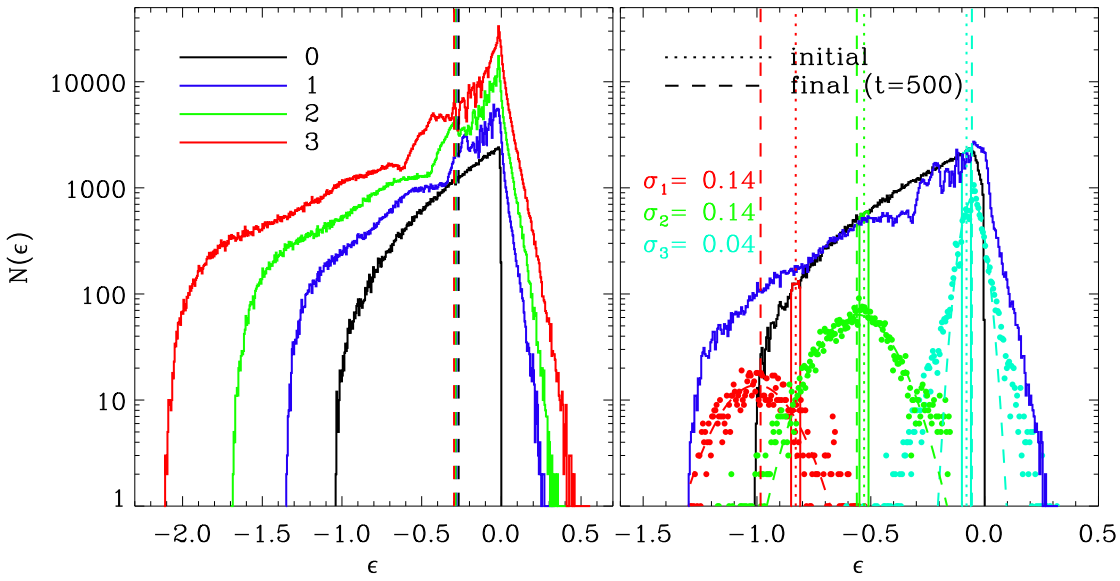

Figure 3. Left panel: Energy distribution for the initial one-component host galaxy and three generations of head-on major mergers (B1ho). The initial distribution (solid black line) is broadened during each merger towards lower and higher (escapers) energies. Finally the most bound particles have about two times their initial binding energy. The mean energy of the total system stays constant (vertical dashed lines). Right panel: Energy distribution for all particles of the progenitor galaxy (black solid line, same as in the left panel) and the same particles after one equal-mass merger (blue solid line). Particles at high (red solid, $-0.85 < \epsilon < -0.81$), intermediate (green solid, $-0.55 < \epsilon < -0.51$) and low initial binding energies (light blue solid, $-0.1 < \epsilon < -0.06$) are highlighted and their energy distribution after the mergers are shown by the dotted distributions. By violent relaxation the two innermost bins are broadened by violent relaxation to Gaussian distributions, with a width of $\sigma = 0.14$. Their mean energies are shifted to lower values (short- and dashed vertical lines). The most weakly bound particles are shifted to higher energies resulting in a significant fraction of escapers.

less systems the total gravitational potential Φ varies with time, which leads to a non-conservation of energy of single particles (Lynden-Bell 1967; Spergel & Hernquist 1992),

$$\frac{d\epsilon}{dt} = -\frac{\partial \Phi}{\partial t}, \tag{5}$$

where ϵ is the energy per unit mass. In accordance with the time dependent virial theorem,

$$\frac{1}{2}\frac{d^2 I}{dt^2} = 2T + V, \tag{6}$$

where I is the moment of inertia tensor, the galaxy will convert its total potential energy V into kinetic energy T and back. In equilibrium, $\ddot{I} = 0$ so $T = -E, V = 2E$, with $E = T + V$ being the total energy. Away from equilibrium the total energy E is constant, but T and V will vibrate about these values, which will widen the differential energy distribution $N(E)$, where $N(E)$ gives the number N of stars within an energy interval $E + dE$.

This evolution is illustrated in the left panel of Fig. 3, where the energy distribution $N(\epsilon)$ broadens with each merger generation very similar to the results reported in Spergel & Hernquist (1992). Using the Ansatz, that violent relaxation can be approximated by scattering effects of single particles, they found an analytic prediction for the final equilibrium configuration for the energy distribution of an equal-mass mergers where the scattering probability functions become Gaussian. In the right panel of Fig. 3 we select particles in three different bins with low ($-0.06 < \epsilon < -0.1$), intermediate ($-0.55 < \epsilon < -0.51$) and high ($-0.85 < \epsilon < -0.81$) initial binding energies. After the final merger, the initially narrow low energy bins are significantly broader and the two most bound bins can be well fitted with a Gaussian of width $\sigma = 0.14$. Bins at lower energies does not become a Gaussian, eventually due to escaping particles. The mean energies of tightly bound particles (red vertical lines) are shifted to even higher binding energies. The temporal evolution of the latter energy bin is detailed in the left panel of Fig. 4. Until $t = 100$ there is little evolution since the galaxy centers are not yet interacting. Then, at the first encounter, the mean binding energy increases strongly and the distribution broadens by a factor of 3 ($\sigma = 0.02 \rightarrow 0.06$). When two galaxies fly apart the mean energy nearly reaches its original value without further broadening ($t = 130$). During the second close encounter, this scenario repeats, i.e. the energy distribution is shifted to higher binding energies accompanied by a strong broadening ($t = 130 \rightarrow 140$), before it oscillates back into a less bound state ($t = 140 \rightarrow 150$). Now the particles reside at slightly higher than initial binding energies. In the right panel of Fig. 4 we depict the evolution of the mean potentials of the three energy bins in Fig. 3, which oscillate strongly for the tightly bound particles (red, green lines) and the energy shifts and broadenings are obviously correlated to the potential fluctuations. On the other hand these fluctuations vanish rapidly, due to phase mixing resulting in incomplete relaxation (Lynden-Bell 1967; Shu 1978). Violent relaxation offers new energy states by deepening the total gravitational potential, into which the most bound particles are scattered making them even more bound. At the same time a fraction of the weakly bound particles reach positive energies and

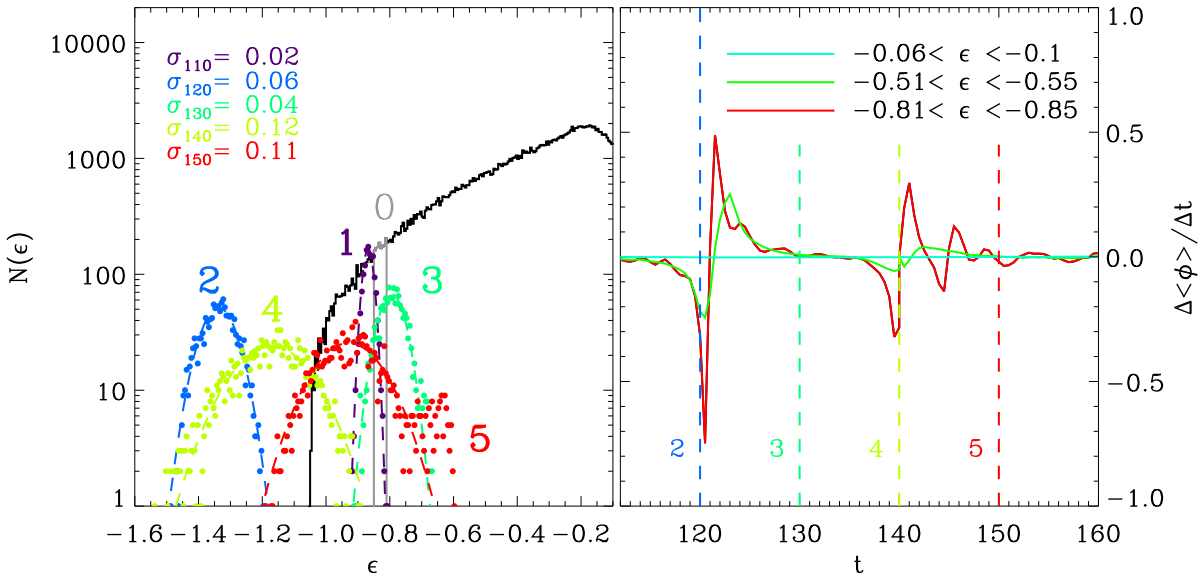

Figure 4. Left panel: Temporal evolution of the energy distribution of highly bound particles (red bin in Fig. 3). The corresponding time evolution during the merger of the average potential of this energy bin (red line) and the two others presented in Fig. 3. The most bound bin shows the strongest fluctuation during the first (2, t = 120) and second (4, t = 140) encounter. The initial distribution at $t = 100$ (0) is slightly broadened to $\sigma_{110} = 0.02$ (1) by two-body relaxation. At the first close encounter $t \approx 120$ (2) the potential rapidly gets deeper (see also right panel), the particles are shifted to higher binding energies and the energy distribution widens to $\sigma_{120} = 0.06$. As the two galaxies fly away from each other, the potential increases and the particles go back to lower binding energies (3) without further broadening of the distribution. During the second close encounter, the process is repeated, i.e. the distribution broadens when the potential gets deeper (4) and moves back to higher energies. After $t = 150$ (5) the central regions show only negligible potential fluctuations and the particle distribution is slowly affected by two-body relaxation. During the merger, the innermost energy bin is broadened from $\sigma = 0.02$ to $\sigma = 0.1$ by violent relaxation. In isolation, this energy bin is only moderately affected by two-body relaxation over the same time interval ($\sigma = 0.02 \rightarrow 0.03$).

escape the potential of the remnant. Two-body relaxation effects for the initial system, evolved in isolation, are much weaker (e.g. $\sigma = 0.02 \rightarrow 0.03$ between $t = 110 \rightarrow 160$).

In the top panel of Fig. 5 we demonstrate, that the overall energy distribution for major mergers of two-component models (solid lines) evolves similar to one-component models, i.e. the tightly bound particles go to states with even higher binding energies and some weakly bound particles become unbound (positive energies). However, with each generation, the number of dark matter particles in the highly bound regions increases more than the number of bulge particles. This behavior can also be seen in the bottom panel of Fig. 5. The fraction of dark matter to bulge particles converges to unity in the central regions. As the energy of the 50% most bound bulge particles, indicated by the small vertical lines at the top of this panel, hardly evolves the intrinsic structure of the system has to change. For example there are only very few dark matter particles in the most bound regions initially, but a non-negligible amount occupies the most bound state of the remnant. This implies that the system undergoes a 'real' change in terms of its dark matter fraction. The fact, that more dark matter than bulge particles wander to higher binding energies is illustrated in Fig. 6 for the first merger of HB1ho. The amount of dark matter scattered to more bound states is larger than the luminous matter for energies $\epsilon \geqslant -1.1$, which is the region where the halo starts to dominate the mass (see top panel Fig. 5).

This demonstrates that violent relaxation rearranges the distributions of dark and luminous matter in energy space, which yields a higher dark matter fraction at the center of the final system. The observable consequences will be discussed in more detail in section 5.2.

3.2 Minor Mergers

In Fig. 7 and the top panel of Fig. 8 we show the total energy distributions (solid lines) for a sequence of head-on, one- and two-component minor mergers, respectively. In both cases nearly all escaping particles originate from the satellites (red dashed-dotted line in both figures), which indicates that violent relaxation only affects the in-falling material and has negligible effects on the distribution of the host galaxy particles. As the satellites are less bound than the host galaxy we find a very high fraction of unbound mass for the final remnants. Furthermore, we can see that almost no accreted particles assemble in the central regions. The loss of binding energy of the most bound particles in both scenarios is caused by two-body effects, which conduct heat into the central high density regions (see also Fig. 1). Combining this shift with the effect, that most satellite particles assemble at low binding energies, results in an increase of the mean binding energies. For the bulge only mergers, the decrease of the mean energy can also be predicted analytically.

The potential energy for a Hernquist sphere is

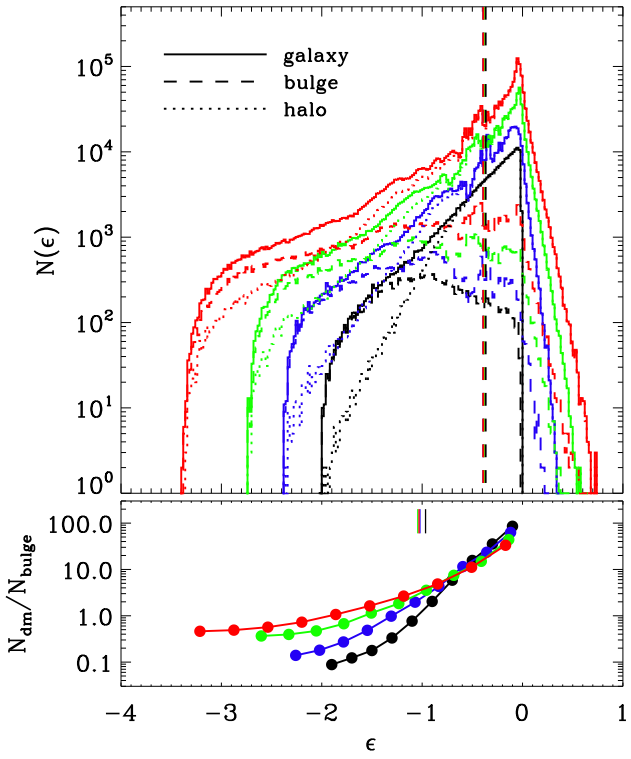

Figure 5. Top panel: Energy distribution for the two-component initial condition (black) and after the first (blue), second (green), and third (red) generation of equal-mass mergers. The solid lines depict the distribution for all particles, the dashed lines for the bulge particles and the dotted lines of the halo particles. The general evolution of the total system is similar to the one-component system (left panel, Fig. 3). The mean binding energy of the systems (vertical dashed lines) stays constant. However, relatively more dark matter particles than bulge particles are scattered to low energies (or higher binding energies), thereby changing the shape of the dark matter energy distribution and increasing the central dark matter fraction (see also Fig. 15). Bottom panel: The ratio of dark matter to bulge particles (or mass as we have equal-mass particles) increases with each merger generation for energies lower than ≈ -0.8 and decreases at higher energies (only bound particles are shown). Finally, there are almost as many dark matter than bulge particles in the innermost bins. The small vertical lines at the top of the panel indicate the energy including 50% of the most bound bulge particles, which stays constant after the first merger.

(Hernquist 1990),

$$W = -\frac{GM^2}{6a}, \tag{7}$$

and according to the virial theorem the total energy of a system in equilibrium is

$$E = \frac{1}{2}W = -\frac{GM^2}{12a}. \tag{8}$$

Additionally we define the mass ratio of accreted to initial host mass $\eta \equiv \frac{M_a}{M_i}$ and the ratio of the according scale radii as $\zeta \equiv \frac{a_a}{a_i}$. Assuming energy conservation for a zero energy orbit, the system's final energy is:

$$E_f = E_i + E_a = -\frac{M_i^2}{12a_i} - \frac{M_a^2}{12a_a} \tag{9}$$

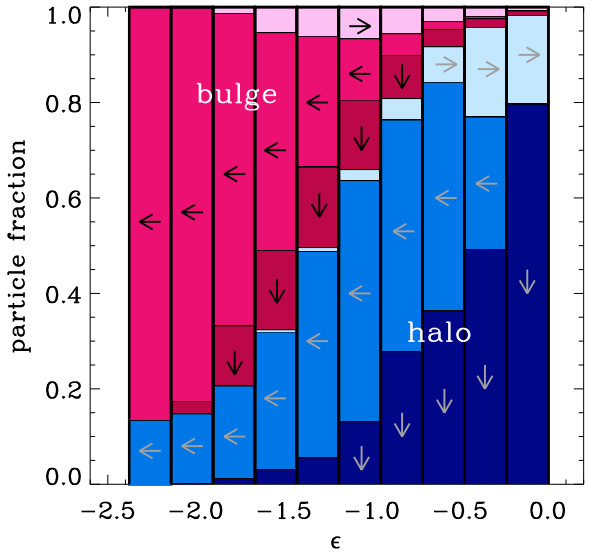

Figure 6. This panel indicates the energetic origin of bulge and halo particles after the first merger (black to blue line in Fig. 5) in terms of particle fractions per energy bin. The lowest energies $\epsilon < -2.0$ were not occupied in the initial system but all particles are scattered down from higher energies during the merger (indicated by $\leftarrow$ and intermediate blue for halo and intermediate red for bulge particles). Energies $\epsilon \geqslant -2.0$ were already initially populated with particles and some of them stay in their initial energy bin (indicated by $\downarrow$ and dark colors). The light blue/red regions show particles scattered up from lower to higher energies (indicated by $\rightarrow$). We predominantly observe downflow in regions where the energy distribution has a positive gradients, i.e. mostly at high binding energies (Fig. 5). This process is driven by violent relaxation and scatters more dark matter than bulge particles into the center increases (bottom panel of Fig. 5). Upflow is seen for regions with negative gradients in the energy distribution, most prominently at the lowest energy bins leading to escapers.

$$= -\frac{M_i^2}{12a_i} - \frac{(\eta M_i)^2}{12\zeta a_i} = -\frac{M_i^2}{12a_i}(1 + \frac{\eta^2}{\zeta}) \tag{10}$$

$$= E_i(1 + \frac{\eta^2}{\zeta}) \tag{11}$$

Furthermore we calculate the mean final energy ε,

$$\varepsilon_f = \frac{E_f}{M} = \frac{E_i(1+\frac{\eta^2}{\zeta})}{M_h + M_s} = \frac{-\frac{M_i^2}{12a_i}(1+\frac{\eta^2}{\zeta})}{M_h(1+\eta)} \tag{12}$$

$$= -\frac{M_i}{12a_i}\left(\frac{1+\frac{\eta^2}{\zeta}}{1+\eta}\right) = -\varepsilon_i\left(\frac{1+\frac{\eta^2}{\zeta}}{1+\eta}\right), \tag{13}$$

where we used the fact that for equal mass particles the total number of particles is equivalent to the total mass M. In the case of an equal mass merger of two identical systems $\eta = \zeta = 1$ and $\varepsilon_f = \varepsilon_i$, i.e. the mean energy of the system stays constant (see also Figs. 3, 5). But for the numerical setup of the first minor merger (B10hoc), where $\eta = 0.1$ and $\zeta = 1$, the final mean energy is $\varepsilon_f = 0.927 \cdot \varepsilon_i$, in agreement with the simulations (Fig.7).

Taking a closer look on the energy distribution of the bulge of the scenario HB10hod (dashed lines, top panel Fig. 8) we can directly see, that most stellar particles accrete at energies $\epsilon > -0.4$, creating an overdensity of bulge parti-

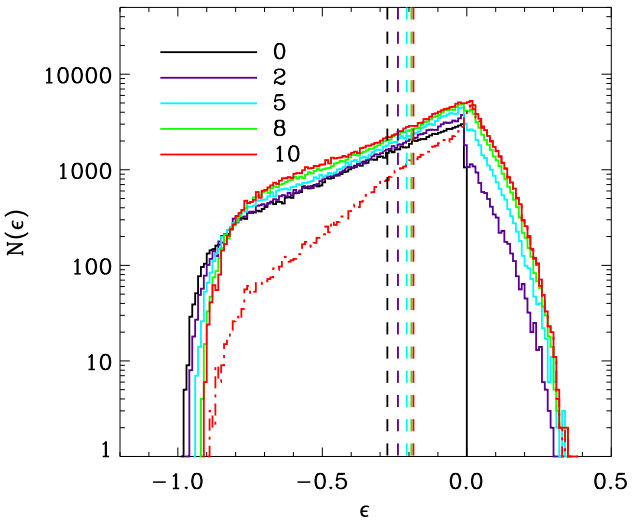

Figure 7. Differential energy distribution for the initial one-component system (black) and two (purple), five (blue), eight (green), and 10 generations of 1:10 head-on mergers (B10hoc). The red dashed-dotted line indicates the energy distribution of all accreted material, which shows that nearly all escapers come from the satellites and nearly no particles assemble at the center. In contrast to equal-mass mergers (left panel, Fig. 4) all bound particles become less bound as the mean binding energy of the systems (vertical dashed lines) decreases with each merger generation.

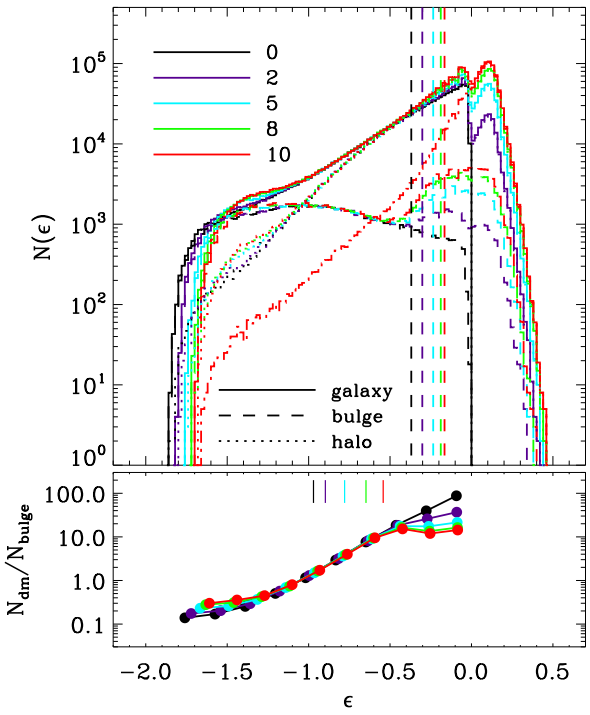

Figure 8. Top panel: Energy distribution for the initial two-component system HB10hod (black) and two (purple), five (blue), eight (green), and 10 (red) generations of 1:10 mergers. The solid lines depict the distribution for all particles, the dashed lines for the bulge particles and the dotted lines of the halo particles. The red dashed-dotted line indicates the energy distribution of all satellite particles. For minor mergers violent relaxation only unbinds satellite particles and the energy distribution of the host is almost unaffected. In contrast to equal-mass mergers (Fig. 5) bound particles become less bound, due to two-body effects. Similar to one-component minor mergers (Fig. 7), the mean binding energy of the systems (vertical dashed lines) decreases with each merger generation. Bottom panel: In stark contrast to equal-mass mergers (Fig. 5) the ratio of dark matter to bulge particles at energies $\epsilon < -0.4$ is unaffected. At higher energies the fraction of (stripped) bulge particles increases. The short vertical lines indicate the energy including 50% of the most bound bulge particles. In contrast to equal mass mergers this energy constantly increases, i.e. the bulge grows into the halo such that the enclosed dark mass increases.

cles. Consequently the ratio of dark matter particles to bulge particles 'decreases' for $\epsilon > -0.4$ (bottom panel of Fig. 8). While this ratio stays constant for all particles with $\epsilon < -0.4$ the lowest binding energy of the 50% most bound particles moves to higher energies and the dark matter fraction increases (see also Fig.15). Altogether we can see, that the dark matter halos of the satellites are dissolved very rapidly in the deep potential well of the host galaxy and efficient tidal stripping leads to a build up of an stellar overdensity at low binding energies.

Comparing the results of minor mergers with either compact or diffuse satellites, the overall evolution stays the same for one- and two-component models. But, as the compact satellites have a higher binding energy, tidal stripping is less efficient and the particles assemble closer to the center. However, the very innermost regions are still hardly affected.

4 VIRIAL THEORY

Going back to virial theory, Naab et al. (2009) presented a simple prediction of how stellar systems evolve during a merger event, which will be extended later on and therefore is repeated briefly. Using the virial theorem and assuming energy conservation we can approximate the ratios of the initial to the final mean square speed $\langle v^2_{\rm i/f}\rangle$, gravitational radius $r_{\rm g,i/f}$ and density $\rho_{\rm i/f}$ of a merging system. According to Binney & Tremaine (2008) the total energy of a system is

$$E_i = K_i + W_i = -K_i = \frac{1}{2}W_i$$
$$= -\frac{1}{2}M_i\langle v_i^2\rangle = -\frac{1}{2}\frac{GM_i^2}{r_{g,i}}, \quad (14)$$

where E_i and M_i are the system's initial total energy and mass. The gravitational radius is defined as

$$r_{g,i} \equiv \frac{GM_i^2}{W_i}, \quad (15)$$

with the total potential energy W_i. Now we define E_a, M_a, $r_{\rm g,a}$ and $\langle v_a^2\rangle$ as the energy, mass, gravitational radius and mean square speed of the accreted system. Additionally to the former defined mass ratio $\eta = M_a/M_i$, $\epsilon = \langle v_a^2\rangle/\langle v_i^2\rangle$ is the dimensionless velocity fraction. By combining these assumptions with equation 14 we obtain

$$\frac{\langle v_f^2\rangle}{\langle v_i^2\rangle} = \frac{(1+\eta\epsilon)}{(1+\eta)}, \quad (16)$$

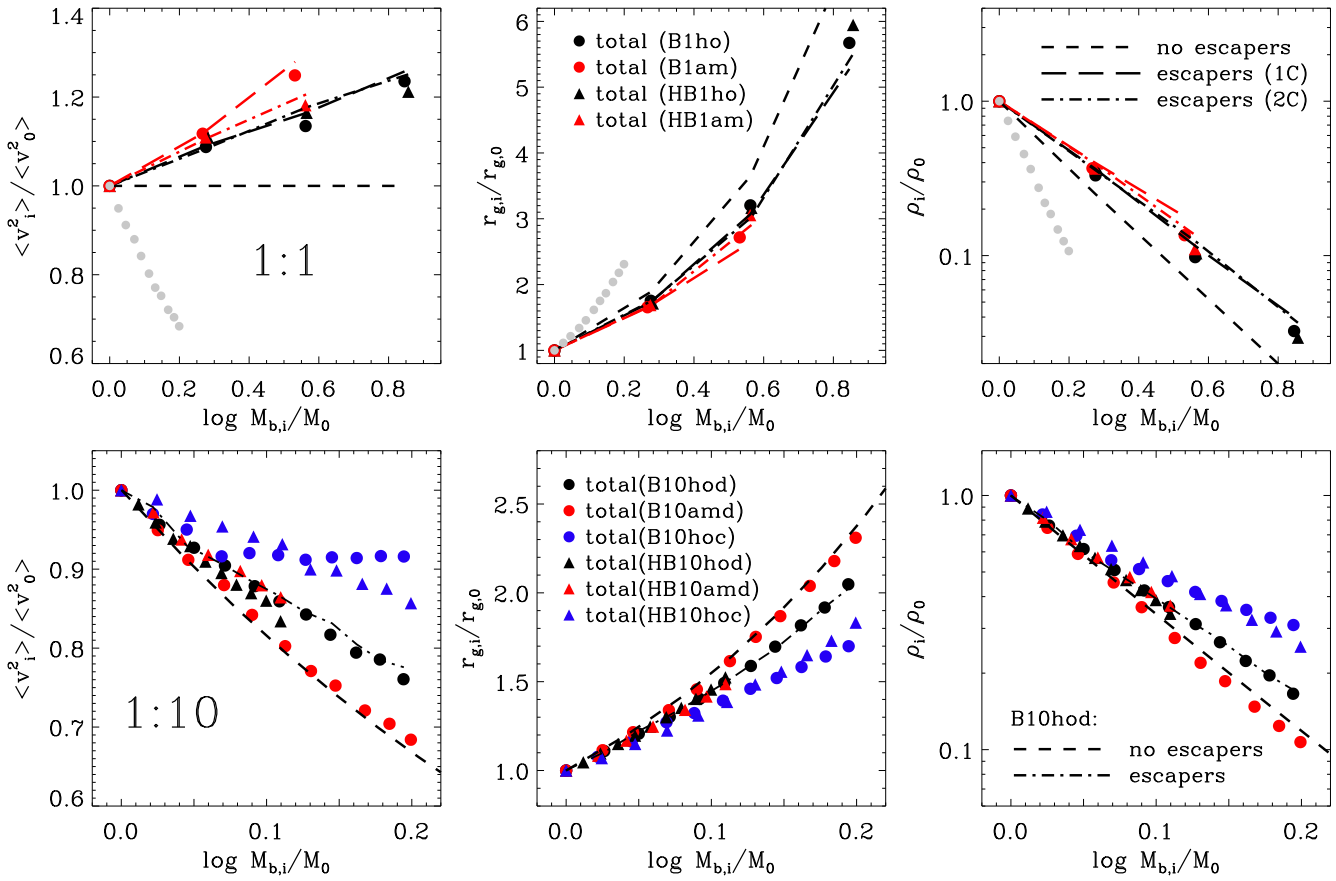

Figure 9. Top panels: Evolution of the mean square speeds (left), the gravitational radii r_g (middle) and the spherical density within r_g (right) for the equal mass merger generations. The circles (triangles) represent the evolution of the one- (two-) component models with (red) and without (black) angular momentum. The black short dashed lines indicate the prediction of Eqs. 16-18. Considering the escaping particles Eqs. 21-23 yield the long dashed lines and the dashed-dotted lines for the one- and two- component scenarios, respectively. For better comparison, the light grey circles highlight the evolution of the minor merger scenario B10amd. Bottom panels: The symbols show the evolution of the minor merger scenarios (see Table 1) for the one- (circles) and two- (triangles) component models with (red) and without (black) angular momentum. The blue circles depict the results, using compact satellite galaxies. The dashed lines are the idealized expectations of Naab et al. (2009) and the dashed dotted lines are accounting for the escapers in the scenario B10hod.

$$\frac{r_{g,f}}{r_{g,i}} = \frac{(1+\eta)^2}{(1+\eta\epsilon)}, \tag{17}$$

$$\frac{\rho_f}{\rho_i} = \frac{(1+\eta\epsilon)^3}{(1+\eta)^5}, \tag{18}$$

for the ratios of the final to initial mean square speed, gravitational radius and density. In the very simple case of an equal mass merger of two identical systems $\eta = \epsilon = 1$, r_g gets doubled (Eq. 17), $\langle v^2 \rangle$ stays constant (Eq. 16) and ρ decreases by a factor of 4 (Eq. 18). If we use equations 7-9 for a minor merger scenario, where $\langle v_a^2 \rangle << \langle v_i^2 \rangle$ and $\epsilon << 1$, the size of the final system can increase by a factor of ~ 4, as $r \propto M^2$. Additionally, the final velocity dispersion and density are reduced by a factor of 2 and 32, respectively. These changes are quantitatively in good agreement with observations.

However, this simple analytic model suffers from a number of limitations, apart from the restrictions to parabolic orbits and collisionless systems. The effect of violent relaxation (Lynden-Bell 1967) in the rapidly changing potential during the merger will scatter particles in energy space, making some more bound and unbinding others from the system, thus energy is not perfectly conserved (see Section 3). Additionally, realistic spheroidal galaxies are composed of two collisionless components, dark and luminous matter with different spatial distributions, which are expected to react differently to a merger event (Naab & Trujillo 2006; Hopkins et al. 2009).

4.1 Major Mergers

Starting with the major mergers, the top left panel of Fig. 9 shows the evolution of the mean square speeds of the one- and two-component equal-mass mergers with the total bound mass of the system. According to Eq. 16 the mean square speed should remain unchanged (dashed line), but obviously it increases with each generation. As a consequence, the growth of the total gravitational radius (top middle panel of Fig. 9) and the density decrease (top right

panel of Fig. 9) are weaker than expected. The same trend was reported by Nipoti et al. (2003, 2009) who correctly argued that the simple analytical prediction is only valid for an idealized case without escaping particles. In the 4th column of Table 1 we show, that the amount of unbound mass after the merger is not negligible and adds up to about 12, 15, 10 and 9% per cent of the total mass for the scenarios B1ho, B1am, HB1ho and HB1am, respectively. The same effect can be seen for the two-component case, where two merger generations with angular momentum have nearly as much mass loss as three generations of the head-on counterparts ($\approx 9\%$ compared to $\approx 10\%$). Looking at the last column of Table 1 we can see that nearly all escaping particles for the two-component models are from the halo, as nearly no stellar mass gets lost ($M_{*,\rm ub} < 3\%$).

We can now revisit the analytic predictions and take the effect of escapers into account (see also Nipoti et al. 2003). The energy equation using the energy of the bound final system E_f and the energy of the escaping particles $E_{\rm esc}$ is

$$E_f + E_{esc} = E_i + E_a. \tag{19}$$

We assume that the escaping particles have essentially zero potential energy, so that

$$E_{esc} = +\frac{1}{2} M_{esc} \langle v_{esc}^2 \rangle. \tag{20}$$

With $\alpha \equiv M_{\rm esc}/M_i$ as the ratio of mass, lost in escapers to initial mass and $\beta \equiv \langle v_{\rm esc}^2 \rangle / \langle v_i^2 \rangle$ as the ratio of the mean square speed of the escapers and the initial system, we can now re-write equations 16 to 18 as

$$\frac{\langle v_f^2 \rangle}{\langle v_i^2 \rangle} = \frac{(1+\eta\epsilon+\alpha\beta)}{(1+\eta-\alpha)}, \tag{21}$$

$$\frac{r_{g,f}}{r_{g,i}} = \frac{(1+\eta-\alpha)^2}{(1+\eta\epsilon+\alpha\beta)} \tag{22}$$

and

$$\frac{\rho_f}{\rho_i} = \frac{(1+\eta\epsilon+\alpha\beta)^3}{(1+\eta-\alpha)^5}. \tag{23}$$

The long dashed (one-component models) and dashed-dotted (two-component models) lines in the top panels of Fig. 9 indicate that the updated analytic predictions are in good agreement with our simulation results. The deviations are less than a few per cent for both models.

The situation becomes more complicated if we separate the velocities of the bulge and the halo component (Fig. 10). The mean square speed of the bulge (green squares) increases more (finally $> 50\%$) with respect to the total system (black squares), whereas the halo (blue squares) speed stays below the total. Here violent relaxation and dynamical friction lead to an energy transfer from the bulge to the halo (see section 3), i.e. the final bulge is more tightly bound than the initial one (see also Boylan-Kolchin et al. 2005 for a discussion of the effect of different orbits).

This effect can be estimated based on the ratio of dark and stellar matter. The total kinetic energy of the system is

$$m_* \langle v_*^2 \rangle + m_{dm} \langle v_{dm}^2 \rangle = m_{tot} \langle v_{tot}^2 \rangle. \tag{24}$$

With $m_{\rm tot} \equiv m_* + m_{\rm dm}$ and introducing $\Delta\langle v_{*/\rm dm}^2 \rangle = \langle v_{*/\rm dm}^2 \rangle - \langle v_{\rm tot}^2 \rangle$ we obtain,

$$m_* \Delta\langle v_*^2 \rangle + m_{dm} \Delta\langle v_{dm}^2 \rangle = 0 \tag{25}$$

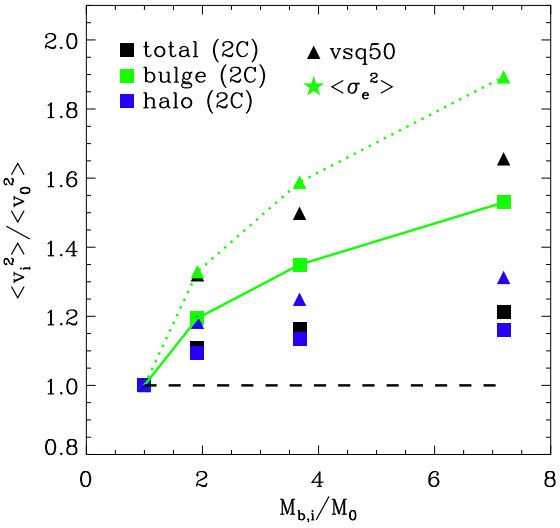

Figure 10. The evolution of the mean square speeds of the total system (black squares), the halo (blue squares) and the bulge (green squares) with bound bulge mass for two-component models on head-on orbits (HB1ho). The more rapid increase of the bulge velocities can be explained by an energy transfer from the halo to the bulge (green solid line, see Eq. 26). At the center this effect is even more efficient, as the mean square speeds within the spherical half-mass radius (corresponding triangles) of the bulge increase more. The dotted green line indicates the expectation of Eq. 26 for the central region.

and the additional growth of the stellar mean square speeds is

$$\Delta\langle v_*^2 \rangle = -\frac{m_{dm}}{m_*} \Delta\langle v_{dm}^2 \rangle. \tag{26}$$

If we now add $\Delta\langle v_*^2 \rangle$ to the mean square speed of the galaxy $\langle v_{\rm tot}^2 \rangle$ we can consistently predict the bulge dispersion (green solid line in Fig. 10).

As violent relaxation scatters some particles into states with higher binding energy, the central region contracts slightly relative to the total system growth (depicted by the gravitational radius). In Fig. 11 we show the radii enclosing the 20, 50 and 80 % most bound particles normalized to the evolution of the gravitational radius. The inner regions expand less, the outer regions more than the gravitational radius. This effect is consistent with the analysis in section 3 and was already described in White (1978, 1979). It leads to a significant non-homology of the system (see also Boylan-Kolchin et al. 2005), as it evolves through successive mergers.

On the other hand, this high central density leads to higher central velocities (triangles, Fig. 10). If we now add $\Delta\langle v_*^2 \rangle$ (Eq. 26) to $\langle v_{\rm tot}^2 \rangle$ for the central regions we again get a very good prediction of the central bulge velocity (green dotted line Fig. 10).

4.2 Minor Mergers

The bottom left panel of Fig. 9 indicates that the mean square speeds of all minor merger hierarchies decrease with increasing mass. In all scenarios with diffuse satellites (black and red symbols), the evolution is very close to the virial

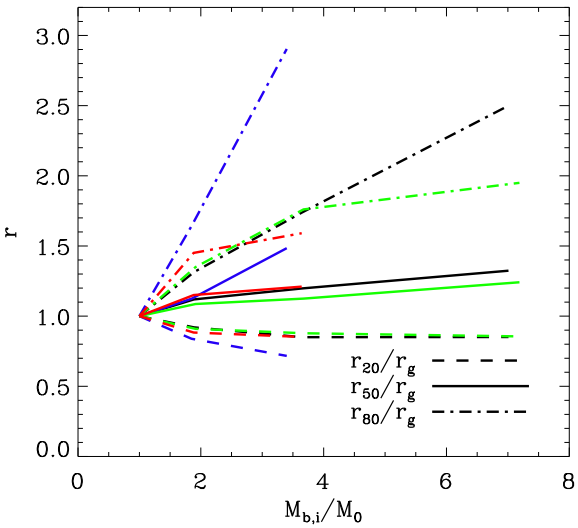

Figure 11. Evolution of the radii enclosing the 20% (dashed), 50% (solid) and 80% (dashed-dotted) most bound particles normalized to the evolution of the gravitational radius , r_g (black: B1ho; blue: B1am; green: HB1ho; blue: HB1am). The inner regions expand less and the outer regions more than the gravitational radius. All ratios are normalized to the initial values.

expectations of Eqs. 16-18 (dashed line), although the mass loss is significant, especially for the two-component models (red and black triangles). In Table 1 we can see that the fraction of escaping particles is up to 35% for HB10hod and around 20% for all other minor merger scenarios. Furthermore, regarding the 2C models, most of the escape fraction is due to the dark matter particles. Going back to the evolution of $\langle v^2 \rangle$, we can see that the corrected prediction of Eq. 21 (dashed-dotted line), which includes the effect of mass loss, perfectly fits the results (e.g. scenario B10hod). Using more compact satellites the final decrease of velocities (blue symbols) is much weaker, because they are more tightly bound. As they have half the scale radius of the diffuse satellites, their binding energies and velocities are two times higher which then doubles the velocity fraction $\epsilon = \langle v_a^2 \rangle / \langle v_i^2 \rangle$ of Eqs. 16-18 and yields a smaller decrease. In combination with the occurring mass loss, this explains the different evolution of the mean square speeds. Nevertheless, in all scenarios the final mean square speeds of the total systems are $10 - 30\%$ lower compared to their initial host galaxies.

The evolution of the gravitational radii (bottom middle panel, Fig. 9) of the six hierarchies evolve according to the mean square speeds, which is not surprising as $r_g \propto 1/\langle v^2 \rangle$ (see Eq. 14). In detail, this means, that the hierarchies with a diffuse satellite show a size increase, which is consistent with the analytic predictions of Eq. 17 (dashed line). As the compact satellites are not able to efficiently decrease the mean square speeds, the gravitational radii grow only marginally. However, for all minor mergers the maximum size growth is around a factor ~ 2.4. For completeness, the bottom right panel illustrates, that the mean density within the gravitational radius evolves according to the gravitational radius ($\rho \propto r_g^{-3}$), i.e. ρ decreases at maximum by 90% (model B10amd, red circles).

5 OBSERVABLES

5.1 Size & Dispersion Evolution

Now we switch focus from theoretical galaxy properties, like the gravitational radii, to directly observable galaxy properties. We compute the effective radius, r_e, as the mean radius including half of the projected bound stellar mass along the three principal axes, the mean projected stellar velocity dispersion, σ_e, within this radius and Σ_e as the mean projected mass surface density within r_e.

5.1.1 Major Mergers

The black triangles in the top left panel of Fig. 12 indicate, that the effective velocity dispersion σ_e^2 for the two-component mergers with head-on orbits (HB1ho) evolves in a similar fashion to the central mean square speeds of the bulge (green triangles Fig. 10), with a final value a factor ~ 1.9 higher than initially. In the case of one-component models, the central region of the remnants just suffer from the contraction effect (Fig. 11) and σ_e^2 is only slightly higher than the mean square speed of the total system (top left panel Fig. 9). This effect is stronger for the scenario with angular momentum orbits. Here, σ_e^2 increases more compared to the head-on case (top left panel Fig. 12) and the escapers change the dispersions of both systems with an additional transfer of kinetic energy from the halo to the bulge particles. (see section 4).

In contrast to the gravitational radii, the observable effective radii of one- and two-component major mergers (top middle panel Fig. 12) follow the simple analytic predictions of Eqs. 16-18, i.e. the effective radius grows proportional to the mass, $r_e \propto M^{\sim 1.0}$. At first this seems surprising as from the virial theorem $r_e \propto M/\sigma_e^2$ and we would expect smaller radii as σ_e^2 increases. Projection effects can be ruled out, as the spherical half-mass radii of the bound remnants evolve similar to r_e and it cannot be an effect of dark matter alone.

As discussed in Nipoti et al. (2003) and Boylan-Kolchin et al. (2005) we also find, that the systems change their internal structure with each merger generation. This non-homology effect can be quantified by the structure parameter c which connects the stellar mass of the systems to its observed size and velocity dispersion

$$M_* = c \cdot \frac{r_e \sigma_e^2}{G}. \quad (27)$$

We use M_* as the bound bulge mass of the remnants to get a comparable value for c of both merger hierarchies (see also Prugniel & Simien 1997; Nipoti et al. 2009). A change in c indicates that the merger remnants do not have a self-similar structure. For the major mergers we find a continuous decrease of c with each merger generation (top panel Fig. 13). The decrease is stronger (a factor of 1.8) for the models including dark matter (triangles) than for the bulge only models (factor of 1.5; circles), which can be explained by an increasing central dark matter fraction. In section 3.1 we have already shown, that this is not just an effect of increasing radii (as argued by Nipoti et al. 2009), but due to violent relaxation. Our results just confirm the findings for major mergers presented in Boylan-Kolchin et al. (2005). The top right panel of Fig. 12 depicts the stellar surface densities,

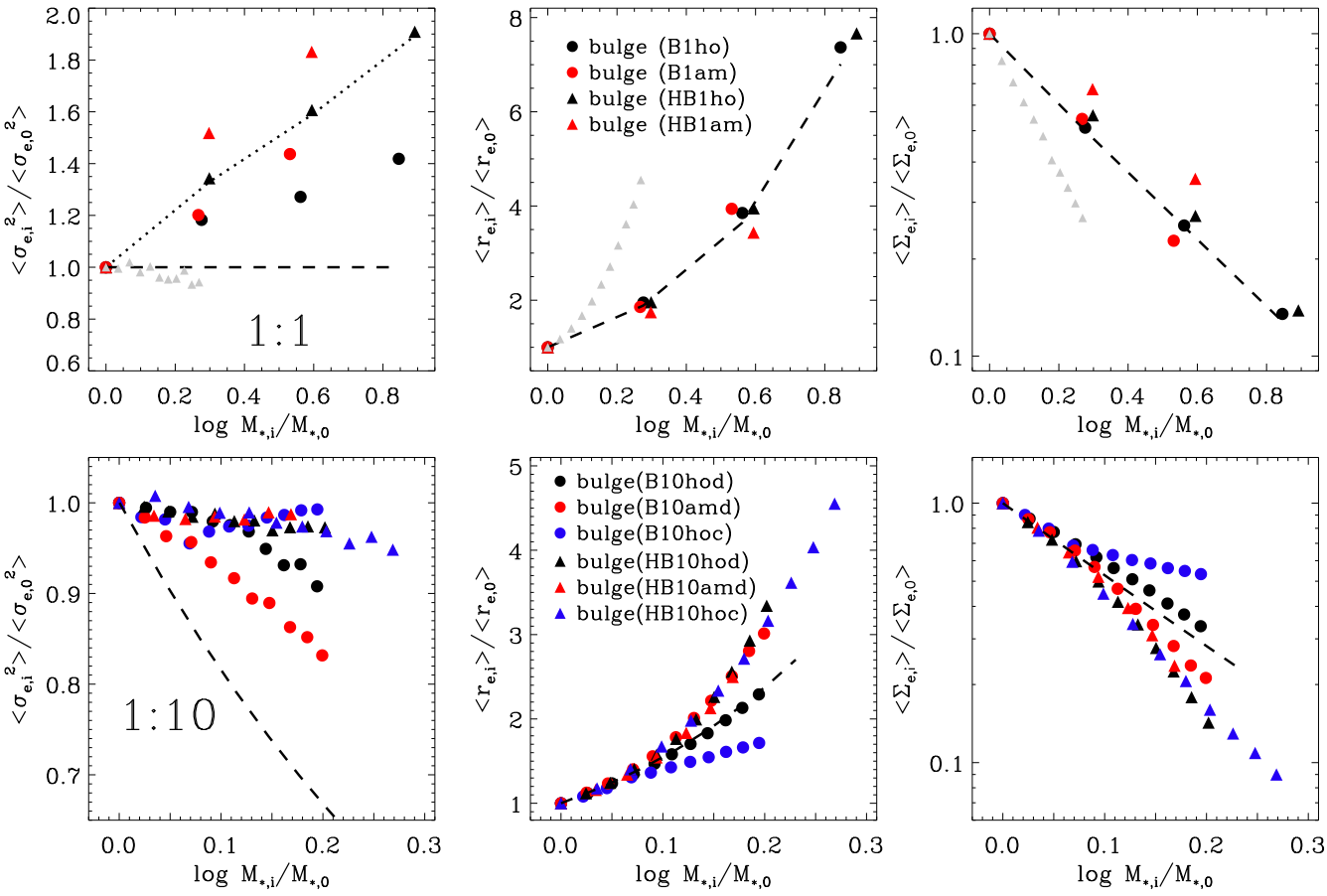

Figure 12. Same as Fig. 9 but for 'observable' bulge properties like the effective line-of-sight velocity dispersions (left panels), the projected half-mass (effective) radii (middle panels) and the effective surface densities (right panels) versus the bound stellar mass normalized to the initial stellar mass. The top panels show the evolution of the major merger and the bottom panels of the minor merger hierarchies, respectively. The light grey triangles in the top panels are the results of the minor merger scenario HB10hoc. The dashed lines indicate the simple analytic predictions (Eqs. 16, 17, and 18) neglecting escapers and energy transfer. The dotted line in the top left panel accounts for both effects fits perfectly σ_e^2 for scenario HB1ho (see also Fig. 10).

which evolve according to r_e and decrease by almost an order of magnitude for a stellar mass increase of a factor ~ 8. For the size increase with mass

$$r_e \propto M_*^{\alpha}, \tag{28}$$

we find $\alpha = 0.8 - 1.0$ for the first equal-mass merger generation, similar to Boylan-Kolchin et al. (2005) for comparable merger orbits. The dispersion evolves as

$$M_* \propto \sigma_e^{\beta}, \tag{29}$$

with $\beta = 3.3 - 5.1$.

5.1.2 Minor Mergers

In the bottom panels of Fig. 12 we show the evolution of σ_e (left), r_e (middle) and Σ_e (right) for all minor mergers. The stellar dispersion σ_e^2 evolves only weakly and does not show the theoretically expected decrease, except for the two bulge-only scenarios with diffuse satellites (B10amd, B10hod).

On the other hand the effective radii r_e (middle panel) grow significantly and in particular for the two-component models the final size can be a factor of 4.5 larger for a mass increase of a about a factor of two. This is more than the maximum value from simple virial expectation (Eq. 17). For all minor merger scenarios of two-component models we get a mass evolution of $r_e \propto M^{\sim 2.4}$, similar to Nipoti et al. (2012) for comparable orbits. This rapid increase is caused by stripped satellite particles which assemble at large radii (see section 3). As an example we show the final stellar surface density distribution of model HB10nod in Fig. 14. The host particles are concentrated at the center similar to their initial distribution. The accreted stellar particles have a much shallower surface density distribution and build up an envelope which dominates at radii $r \geqslant r_e$. The structure parameter evolves strongly and very similar for all two-component systems. Its evolution mainly reflects the rapid size growth (black, red and blue triangles in the bottom panel of Fig. 13). This strong evolution is also seen for the effective surface densities (bottom right panel of Fig. 14), which can decrease at maximum by an order of magnitude for a size increase of a factor of two.

For bulge-only minor mergers scenarios the structural

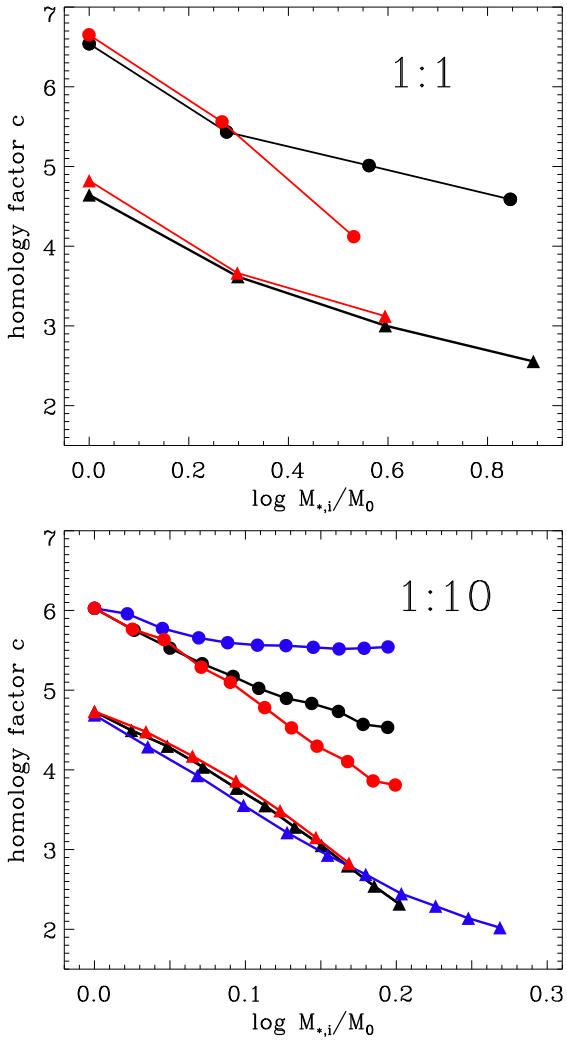

Figure 13. Evolution of the structure parameter c relating the stellar mass with the effective radius and velocity dispersion $c = (r_e\sigma^2)/(M_*G)$ with bound stellar mass for 1:1 mergers (top panel) and 1:10 mergers (bottom panel). For all cases c decreases and homology is not preserved. In particular the structure of the two-component minor mergers (triangles) changes rapidly with added stellar mass. The colors and symbols in both panels are the same as in Fig. 9.

changes depend on the initial conditions. Minor mergers with compact satellites (B10hoc) evolve nearly self-similar with only mild changes in the structural parameter (bottom panel of Fig. 13) and a weak evolution in σ_e, r_e and Σ_e (bottom panels of Fig. 12). The observable parameters evolve very similar to the theoretical ones (bottom panels of Fig. 9). The other two bulge only minor merger models have weakly bound satellites, which already loose most of their material in the outer regions of the host galaxy and also build up an extended envelope with a corresponding change in structural properties (see also black and red circles in Fig. 13). On the other hand, the development of an extended envelope boosts the size growth of a system. As the sequence B10amd with an angular momentum orbit needs more time

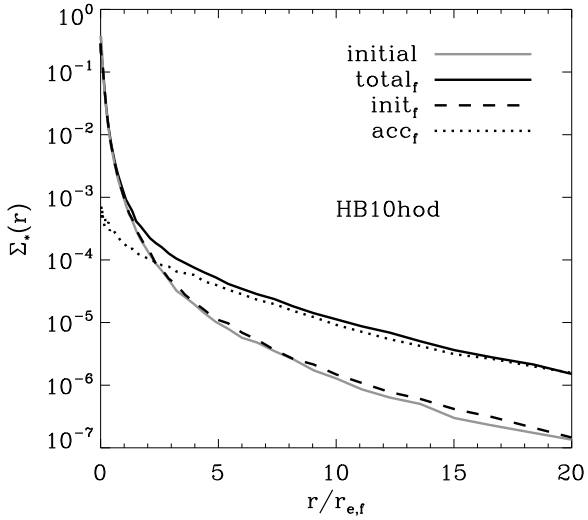

Figure 14. Surface mass densities of bulge particles along the major axis, normalized to the final effective radius for head-on minor mergers (model HB10hod) of two-component models. The grey solid line indicates the initial host stellar surface density, which almost remains unchanged (black dashed line). Most of the satellite stars (dotted line) assemble with a shallower surface density profile and dominate the outer parts of the total surface density of the remnant at $r > r_e$ (black solid line). The accreted stars are responsible for the rapid size growth.

until the final coalescence, it suffers more from tidal stripping and builds up the most extended envelope of all bulge only models, which then results in the highest size growth (red circles, Fig. 12). This implies, that the calculation of σ_e also includes particles outside the innermost regions, where the velocities are lower and the velocity dispersion within the effective radius decreases.

5.2 Dark Matter Fractions

As already discussed in section 3 mergers of bulge-halo systems in general increase the central dark matter fractions. For major mergers this process is driven by violent relaxation changing the composition of the remnants whereas in minor mergers structure is almost unchanged but the 'ruler' which is the size of the stellar system covers larger radii with initially higher dark matter contributions. The 'observable' quantity here is the dark matter fraction within the stellar half-mass radius which is presented in Fig. 15 (see also Barnabè et al. 2011). For major mergers the dark matter fraction increases with every merger generation, probably saturating for later generations. A stellar mass increase of a factor two results in an increase of the dark matter fractions by $\sim$ 25% for the first generation and $\sim$ 18% and $\sim$ 5% for the second and third generation, respectively. For minor mergers the increase in dark matter fraction is almost linear to the mass increase and significantly more dramatic than for major mergers. A mass increase of a factor two results in an increase of the dark matter fraction by $\sim$ 80%, which is three times more than for major mergers, without any signature for saturation. This implies that merging, minor mergers in particular, is a significant driver for the increase

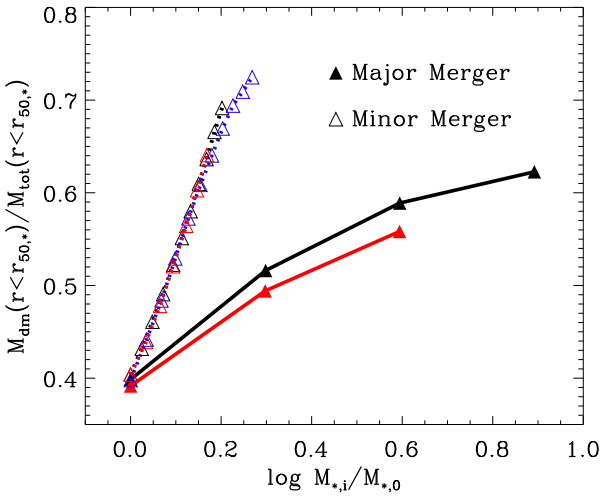

Figure 15. The dark matter fraction within the spherical half-mass radius of the bulge, $f_{\rm dm} = M_{\rm dm}/(M_{\rm dm} + M_*)$, versus the bound stellar mass of the two-component major (filled triangles) and minor (open triangles) merger remnants. The colors are the same as in Fig. 9. For major mergers, the dark matter fraction increases by 50% for a mass increase of a factor ~ 8 (25% for a mass increase of a factor ~ 2). Due to the rapid increase of the effective radii, the dark matter fraction of the minor mergers increases by almost 80% for a mass increase of less than a factor 2.

of dark matter in galaxies which had to be more baryon dominated in the past if their assembly history was dominated by stellar merging. We note that for minor mergers the increase in dark matter fraction seems to be roughly proportional to the mass growth.

5.3 Velocity Dispersion Profiles

One prediction of violent relaxation is that during a merger the system evolve to a state of higher entropy and the more complete the violent relaxation is the higher the entropy, eventually approaching the isothermal sphere. In reality, phase mixing damps the potential fluctuations of a merger rapidly, and violent relaxation is incomplete, which results in a final equilibrium distribution which does not reach the highest possible entropy state (see White & Narayan (1987) for a detailed discussion on maximum entropy states in galaxies).

In Fig. 16 we show the radial velocity dispersion profiles for major mergers of one-component systems. The radial velocity dispersion of the final remnant (red line) can be well fitted with a Jaffe profile (Jaffe 1983) over a large radial range. In the inner parts this profile resembles the singular isothermal sphere (Tremaine et al. 1994). The corresponding changes of the structural parameter (see section 4) are also given in the same figure. In the case of two-component models (Fig. 17) we find the same result, i.e. the total (solid line) and also the bulge profile (dotted line) approach a Jaffe profile. Spergel & Hernquist (1992) find the same trend for only one generation of a head-on equal mass merger. This leads to the following tentative conclusion. The evolution of

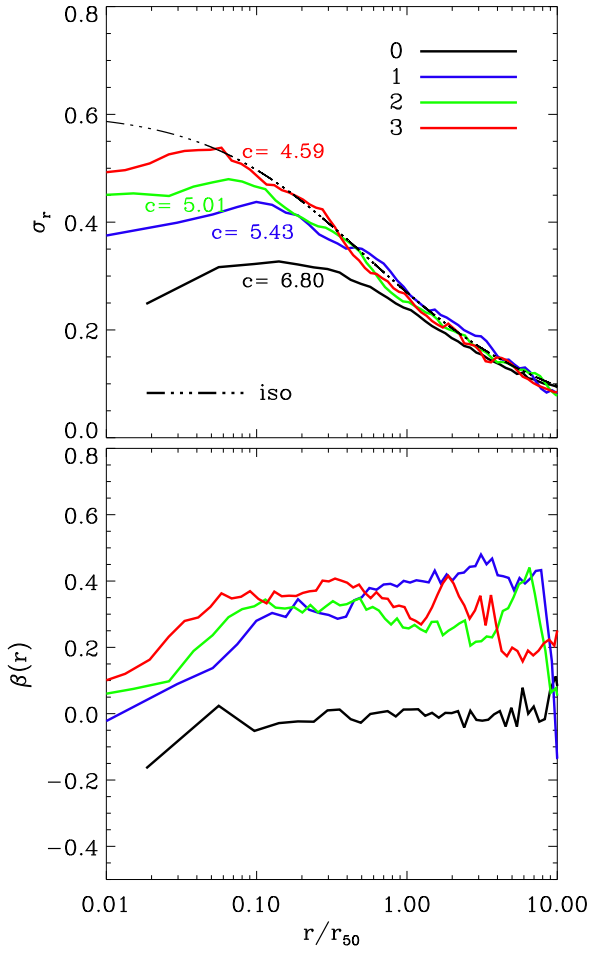

Figure 16. Top: Final radial velocity dispersions of the one-component merger generations (B1ho). The colors depict the different generations. The dashed-dotted line indicates the velocity dispersion of a Jaffe profile, which has the same scale length and mass as the last remnant. The latter profile resembles the inner parts of the singular isothermal sphere which is a very good fit to our last merger remnant. As the structure parameter c decreases with each generation homology is not preserved. Bottom: Anisotropy parameter β (eq. 30) against radius of three generations of one-component equal-mass mergers. As $\beta > 0$ for higher generations the remnants become radially anisotropic over the whole radial range. The half-mass radius r_{50} is the radius of the sphere, which includes half of the bound system mass.

the merger remnants towards a more isothermal distribution is not unexpected since the entropy cannot decrease in any collisionless process. However, by how much, or if at all, the entropy increases is hard to anticipate since, formally, there exists no maximum-entropy state for each merger generation. The comparison with the Jaffe model shows that violent relaxation in the centre is very effective. From one merger generation to the next both the total mass and energy change. This provides new phase-space states with ever higher binding energy that are populated by violent relaxation. As a result, the nearly isothermal region of the remnant extends deeper into the centre after each generation.

In the bottom panels of Figs. 16, 17 we can see that the initially isotropic remnants become radially anisotropic for

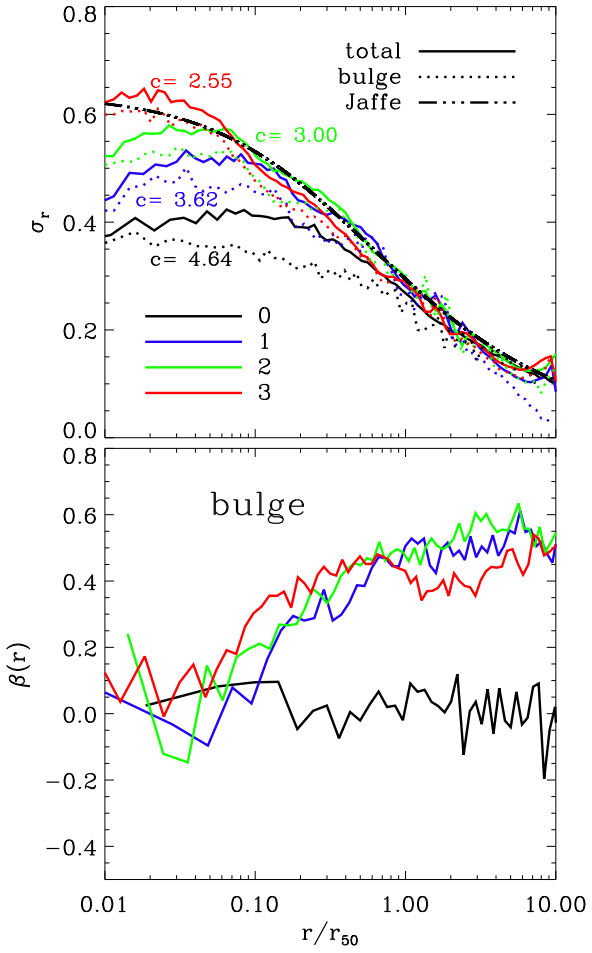

Figure 17. The top panel shows the same as in Fig. 16 for the total remnants (solid lines) and the bound bulges (dotted lines) of the head-on two-component mergers (HB1ho). The bottom panel depicts the anisotropy parameter for the bulge. Here, r_{50} is the spherical half mass radii of the total (top) and stellar (bottom) bound remnants. If the bulge is embedded in a dark matter halo, β is slightly higher compared to the one-component case.

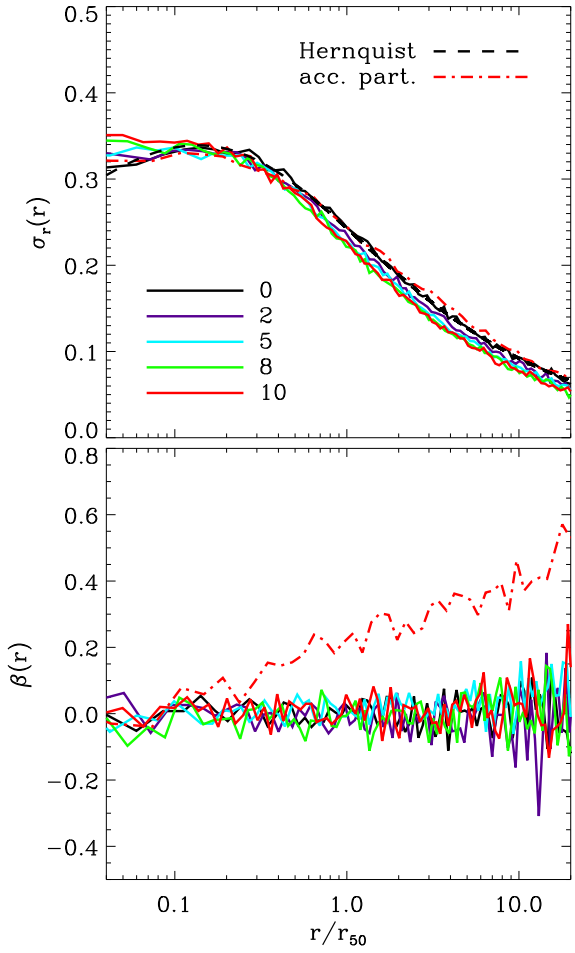

Figure 18. Top panel: The radial velocity dispersion for the head-on minor mergers of one-component models (B10hoc) stays constant over most of the radial range. Only in the very central regions, it increases slightly with each generation. The black dashed line is the initial Hernquist profile and the red dashed-dotted line the velocity dispersion of all bound accreted particles. Bottom panel: For the whole bound remnant, the velocity distribution stays perfectly isotropic, as the anisotropy parameter β stays zero. Looking at the accreted material (red dashed-dotted line) , it gets radially anisotropic with increasing radius. In both panels the radius is normalized to the spherical half-mass radius of the bound system.

most of the galaxy $r > 0.1r_{50}$. Already after the first merger the anisotropy parameter (Binney & Tremaine 2008)

$$\beta = 1 - \frac{\sigma_\theta^2 + \sigma_\phi^2}{2\sigma_r^2}. \tag{30}$$

becomes positive indicating radial anisotropy. This is not surprising, as we only use orbits with very small or zero pericenter distances (see also Boylan-Kolchin & Ma 2004).

Next we focus on the evolution of the velocity dispersion profiles (Figs. 18, 19) of the minor mergers. From the previous analysis we have seen that violent relaxation has no significant influence on the central regions of the host galaxies. This is also reflected in the weak evolution of the central radial velocity dispersion profiles $\sigma_r(r)$ of the one- and two-component minor mergers (top panels of Figs. 18, 19). In particular for the one-component scenario (e.g. B10hoc in top panel of Fig. 18) $\sigma_r(r)$ keeps the initial Hernquist profile shape (black dashed line) over the whole radial range. Furthermore, as $\beta(r) \sim 0$ (bottom panel Fig. 18) all remnants (solid lines) stay isotropic. The accreted stars only show an increasing radial anisotropy $\beta(r) > 0$ with increasing radius. The aforementioned effects are similar for all one-component minor mergers, but slightly less pronounced in the cases with angular momentum.

The merger remnants of two-component models (top panel Fig. 19) also indicate characteristics which are consistent with the evolution of their differential energy distribution (Fig. 8). The central regions are hardly affected and therefore, the total velocity dispersion profile (solid lines in the top panel of Fig. 19) and the one of the halo stay constant. The accreted stellar particles create a bump in the energy distribution (dashed lines in Fig. 8), which gets more and more prominent with each subsequent generation. These accreted particles induce an increasing stellar velocity dis-

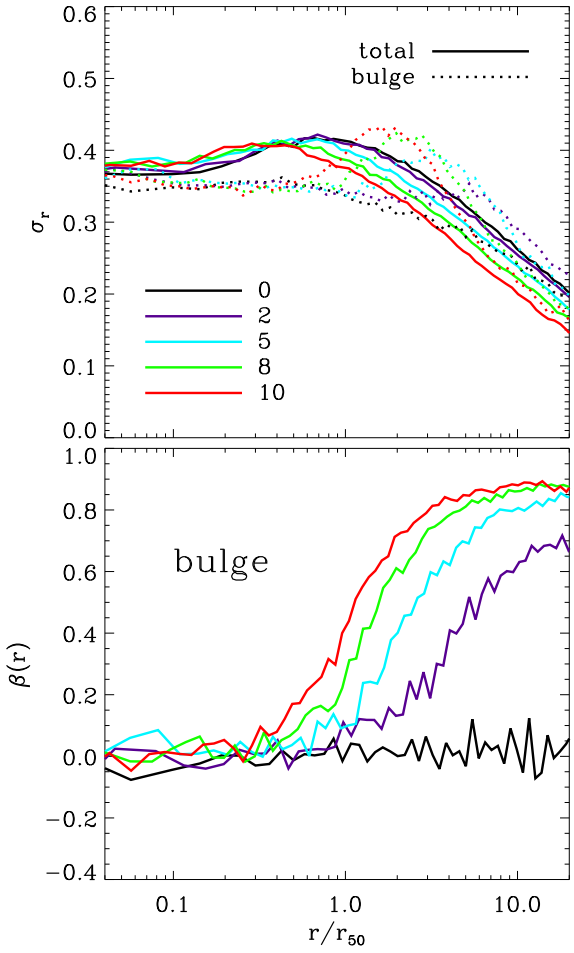

Figure 19. Top panel: The radial velocity dispersion of the total system (solid lines) for the head-on minor mergers of two-component models (HB10hod) stays constant over the whole radial range. The dispersion of the bulge system (dotted line) builds up a prominent peak which comes from the accreted material, which is mostly affected by dynamical friction. The radii are normalized to the spherical half-mass radius of the bulge. Bottom panel: The anisotropy parameter of the bulge velocities gets radially biased at radii greater than the spherical half-mass radii of the bulge.

persion at radii larger than the spherical half-mass radius r_{50} (dotted lines, top panel Fig. 19). As the final coalescence of the stellar component in the two-component scenario is on radial orbits, independent of the initial conditions (see also González-García & van Albada (2005)), the anisotropy parameter becomes radially biased for all of our minor mergers (e.g. HB10hod, bottom panel of Fig. 19). This effect only occurs in the simulation including a dark matter halo, because then the angular momentum of the in-falling satellite is lost before the final merger, due to enhanced dynamical friction. Hence, most of the stellar particles approach on radial orbits and are, during the final coalescence, stripped before reaching the center. If we use the compact satellites, the overall trend does not change, but more material reaches the center, as the particles are more tightly bound and suffer less from tidal stripping.

6 SUMMARY & DISCUSSION

In this paper we have presented a series of numerical simulations of major (mass-ratio of 1:1) and minor (mass-ratio of 1:10) mergers of spherical, isotropic early-type galaxies. The model galaxies consist of a bulge (one-component model) or a bulge embedded in a massive dark matter halo (two-component model). After describing the procedure to set up the initial conditions we have demonstrated the stability of the one- and two-component galaxy models. By analysing the merger simulations we have identified two different processes dominating the evolution in sizes, velocity dispersion and dark matter fraction in major and minor mergers, respectively.

Violent relaxation is the dominant mixing process in major mergers, broadening the energy distribution, unbinding weakly bound particles and making bound particles more bound. As a result the stellar velocity dispersion increases and the size increase is weaker ($r \propto M^{\alpha}$ with $\alpha < 1$) than predicted from simple virial arguments, an effect already reported by Nipoti et al. (2003). We present an analytical estimate for the size and dispersion evolution taking the mass-loss into account and also separating the effect on the dispersion of the stars and the dark matter halo for the two-component models. The physical origin of the increase of the dark matter fraction in equal-mass mergers reported by Boylan-Kolchin et al. (2005) have been identified. In the transition region of luminous to dark matter domination, relatively more dark matter particles are scattered from higher to lower energies (becoming more tightly bound). This rearrangement is driven by violent relaxation and leads to an increase of the the dark matter fraction within the observable effective radius of about 25 per cent for one equal-mass merger, equivalent to a stellar mass increase of a factor of two.

Stripping of stars from the low mass satellites is the dominant process driving the size evolution in minor (1:10) mergers. The stripped stars are predominantly deposited at large radii, leaving the central structure of the host galaxies almost unchanged. This process was proposed to be the origin of abundance gradients in elliptical galaxies (Villumsen 1983). The assembly of a 'halo' of accreted stars leads to a rapid increase of the effective radius. In systems with dark matter halos the stripped stars, with radially biased velocity dispersion, are now populating regions where the host galaxy was previously dominated by dark matter. As a result the bulge size increase for two-component minor mergers is more rapid than predicted from simple analytical estimates ($r \propto M^{\alpha}$ with $\alpha > 2$). This results in an about three times stronger increase of the dark matter fraction within the stellar half-mass radius (compared to equal-mass mergers) for a mass increases of a factor of two.

Observational estimates of van Dokkum et al. (2010) indicate a size growth of $r_e \; \alpha \; M^{2.04}$, which would be qualitatively consistent with two-component minor merger scenarios. We have to note, however, that the exact details will depend on the structure of the galaxies, the merger orbits and the mass and extend of the dark matter halos etc., a parameter space too large to cover in this study. Nipoti et al. (2009, 2012) followed a similar approach in a cosmologically motivated context and found a much weaker size typical size increase ($r_e \propto M^{1.09}$). A possible reason for this discrepancy

is, that they averaged over all major and minor mergers. Additionally, they used a steeper central slope for the stellar density profiles leading to more bound satellites being even more compact than our satellites which lie on an extrapolation of the $z = 2$ mass-size relation of Williams et al. (2010).

As we, and others before, have shown, increasing dark matter fractions will change the ratio of dynamical to stellar mass. This effect, if relevant in nature, will contribute to the observed tilt of the fundamental plane, in addition to stellar populations and structural non-homology (e.g. Nipoti et al. 2003; Boylan-Kolchin et al. 2005; Ciotti et al. 2007; Graves & Faber 2010; Thomas et al. 2011; Toft et al. 2012). We also agree with Nipoti et al. (2009) that the increase of the dark matter fraction is stronger for minor mergers and for this scenario is dominated by the rapid size growth. But in contrast to Nipoti et al. (2009), we find that the central dark matter fraction of equal-mass mergers represents a 'real' change in the internal structure caused by violent relaxation and not by the size growth of the galaxies. More massive galaxies, which are expected to have acquired more stars in late mergers (De Lucia et al. 2006; Khochfar & Silk 2006; Oser et al. 2010; Moster et al. 2012; Laporte et al. 2012), will therefore have higher dark matter fractions (see also Lackner & Ostriker (2010) for a detailed discussion). This picture is in agreement with recent high-resolution cosmological simulations (e.g. Johansson et al. 2012) and might explain the potentially high dark matter fractions measured for elliptical galaxies in particular if the merger history was dominated by minor mergers (e.g. Lackner & Ostriker 2010; Barnabè et al. 2011; Auger et al. 2010). This explanation for the tilt of the fundamental plane is traditionally degenerate with uncertainties in the initial stellar mass functions. Some recent studies imply that the stellar mass-to-light ratio rises as a function of the stellar mass of the galaxies, leaving relatively little room for the presence of dark matter at the center of massive galaxies (van Dokkum & Conroy 2010; Cappellari 2012; Conroy & van Dokkum 2012; van Dokkum & Conroy 2012; Ferreras et al. 2012). If true this might be in considerable tension with cosmological simulations of massive galaxies and a merger driven size growth scenario - supported by massive dark matter halos - in general.

The global mean square speeds of the systems decrease in minor mergers but the 'observed' effective line-of-sight velocity dispersions hardly change. The most promising realistic scenario investigated here, the two-component minor mergers, shows a relatively weak decrease in the effective velocity dispersion, eventually too weak to explain the available observational data (Cenarro & Trujillo 2009; van Dokkum et al. 2009; van de Sande et al. 2011b; Toft et al. 2012). However, reliable spectroscopic measurements are only available for few galaxies so far and the constraints are weaker than for the size evolution. In addition, studies like Cenarro & Trujillo (2009) compared galaxies at a fixed stellar mass at different redshifts not taking the expected mass increase into account, i.e. massive galaxies at high redshift should be compared to even more massive galaxies (with higher dispersions) at present. In addition, details of the model, like mass concentration, orbits etc. will also affect the dispersion evolution. It is, however, reassuring that more realistic cosmological simulations, which also include a dissipative component, are able to reproduce the observed dispersion evolution (e.g. Oser et al. 2012).

In summary our work shows that dissipationless dry minor mergers of bulges embedded in dark matter halos can significantly increase the sizes of a compact spheroids resembling high-redshift systems. As the predictions for size growth are even above the observed values small amount of gas, which is known to reduce the size growth (Covington et al. 2011; Hopkins et al. 2008), would perhaps not be enough to invalidate this scenario. Recent simulations of galaxy formation in a full cosmological context seem to support the conclusions drawn from the idealized simulations presented here with respect to the evolution of sizes, dispersions, abundance gradient as well as dark matter fractions (Naab et al. 2007, 2009; Joung et al. 2009; Oser et al. 2010, 2012; Feldmann et al. 2010, 2011; Johansson et al. 2012; Lackner et al. 2012).

ACKNOWLEDGMENTS

We thank Peter Johansson and Simon White for helpful discussions. This research was supported by the DFG cluster of excellence Origin and Structure of the Universe and the DFG priority program SPP 1177.

REFERENCES

Arad I., Johansson P. H., 2005, MNRAS, 362, 252
Auger M. W., Treu T., Bolton A. S., Gavazzi R., Koopmans L. V. E., Marshall P. J., Moustakas L. A., Burles S., 2010, ApJ, 724, 511
Barnabè M., Czoske O., Koopmans L. V. E., Treu T., Bolton A. S., 2011, MNRAS, 415, 2215
Bell E. F., Naab T., McIntosh D. H., Somerville R. S., Caldwell J. A. R., Barden M., Wolf C., Rix H.-W., Beckwith S. V., Borch A., Häussler B., Heymans C., Jahnke K., Jogee S., Koposov S., Meisenheimer K., Peng C. Y., Sanchez S. F., Wisotzki L., 2006, ApJ, 640, 241
Bell E. F., Phleps S., Somerville R. S., Wolf C., Borch A., Meisenheimer K., 2006, ApJ, 652, 270
Bezanson R., van Dokkum P. G., Tal T., Marchesini D., Kriek M., Franx M., Coppi P., 2009, ApJ, 697, 1290
Binney J., Tremaine S., 2008, Galactic Dynamics: Second Edition
Bournaud F., Chapon D., Teyssier R., Powell L. C., Elmegreen B. G., Elmegreen D. M., Duc P.-A., Contini T., Epinat B., Shapiro K. L., 2011, ApJ, 730, 4
Bournaud F., Jog C. J., Combes F., 2007, A&A, 476, 1179
Boylan-Kolchin M., Ma C., Quataert E., 2005, MNRAS, 362, 184
Boylan-Kolchin M., Ma C.-P., 2004, MNRAS, 349, 1117
Buitrago F., Trujillo I., Conselice C. J., Bouwens R. J., Dickinson M., Yan H., 2008, ApJ, 687, L61
Cappellari M., di Serego Alighieri S., Cimatti A., Daddi E., Renzini A., Kurk J. D., Cassata P., Dickinson M., Franceschini A., Mignoli M., Pozzetti L., Rodighiero G., Rosati P., Zamorani G., 2009, ApJ, 704, L34
Cappellari M. e. a., 2012, Nature, 484, 485
Cenarro A. J., Trujillo I., 2009, ApJ, 696, L43

Cimatti A., Cassata P., Pozzetti L., Kurk J., Mignoli M., Renzini A., Daddi E., Bolzonella M., Brusa M., Rodighiero G., Dickinson M., Franceschini A., Zamorani G., Berta S., Rosati P., Halliday C., 2008, A&A, 482, 21
Cimatti A., Nipoti C., Cassata P., 2012, arXiv:1202.5403
Ciotti L., 1996, ApJ, 471, 68
Ciotti L., Lanzoni B., Volonteri M., 2007, ApJ, 658, 65
Cole S., Lacey C. G., Baugh C. M., Frenk C. S., 2000, MNRAS, 319, 168
Conroy C., van Dokkum P., 2012, arXiv:1205.6473
Cooper M. C., Griffith R. L., Newman J. A., Coil A. L., Davis M., Dutton A. A., Faber S. M., Guhathakurta P., Koo D. C., Lotz J. M., Weiner B. J., Willmer C. N. A., Yan R., 2012, MNRAS, 419, 3018
Covington M. D., Primack J. R., Porter L. A., Croton D. J., Somerville R. S., Dekel A., 2011, MNRAS, 415, 3135
Daddi E., Renzini A., Pirzkal N., Cimatti A., Malhotra S., Stiavelli M., Xu C., Pasquali A., Rhoads J. E., Brusa M., di Serego Alighieri S., Ferguson H. C., Koekemoer A. M., Moustakas L. A., Panagia N., Windhorst R. A., 2005, ApJ, 626, 680
Damjanov I., McCarthy P. J., Abraham R. G., Glazebrook K., Yan H., Mentuch E., LeBorgne D., Savaglio S., Crampton D., Murowinski R., Juneau S., Carlberg R. G., Jørgensen I., Roth K., Chen H.-W., Marzke R. O., 2009, ApJ, 695, 101
De Lucia G., Springel V., White S. D. M., Croton D., Kauffmann G., 2006, MNRAS, 366, 499
de Vaucouleurs G., 1948, Annales d'Astrophysique, 11, 247
Dehnen W., 1993, MNRAS, 265, 250
Dehnen W., 2001, MNRAS, 324, 273
Dekel A., Sari R., Ceverino D., 2009, ApJ, 703, 785
Faber S. M., Jackson R. E., 1976, ApJ, 204, 668
Farouki R. T., Shapiro S. L., Duncan M. J., 1983, ApJ, 265, 597
Feldmann R., Carollo C. M., Mayer L., 2011, ApJ, 736, 88
Feldmann R., Carollo C. M., Mayer L., Renzini A., Lake G., Quinn T., Stinson G. S., Yepes G., 2010, ApJ, 709, 218
Ferré-Mateu A., Vazdekis A., Trujillo I., Sánchez-Blázquez P., Ricciardelli E., de la Rosa I. G., 2012, MNRAS, p. 2790
Ferreras I., La Barbera F., de Carvalho R. R., de la Rosa I. G., Vazdekis A., Falcon-Barroso J., Ricciardelli E., 2012, arXiv:1206.1594
Franx M., van Dokkum P. G., Schreiber N. M. F., Wuyts S., Labbé I., Toft S., 2008, ApJ, 688, 770
Genel S., Genzel R., Bouché N., Sternberg A., Naab T., Schreiber N. M. F., Shapiro K. L., Tacconi L. J., Lutz D., Cresci G., Buschkamp P., Davies R. I., Hicks E. K. S., 2008, ApJ, 688, 789
González-García A. C., van Albada T. S., 2005, MNRAS, 361, 1043
Graves G. J., Faber S. M., 2010, ApJ, 717, 803
Guo Q., White S. D. M., 2008, MNRAS, 384, 2
Hernquist L., 1990, ApJ, 356, 359
Hopkins P. F., Bundy K., Hernquist L., Wuyts S., Cox T. J., 2010, MNRAS, 401, 1099
Hopkins P. F., Bundy K., Murray N., Quataert E., Lauer T. R., Ma C., 2009, MNRAS, 398, 898
Hopkins P. F., Cox T. J., Hernquist L., 2008, ApJ, 689, 17
Hopkins P. F., Hernquist L., Cox T. J., Keres D., Wuyts S., 2009, ApJ, 691, 1424
Jaffe W., 1983, MNRAS, 202, 995
Jiang F., van Dokkum P., Bezanson R., Franx M., 2012, arXiv:1203.1317
Johansson P. H., Naab T., Ostriker J. P., 2009, ApJ, 697, L38
Johansson P. H., Naab T., Ostriker J. P., 2012, arXiv:1202.3441
Joung M. R., Cen R., Bryan G. L., 2009, ApJ, 692, L1
Kazantzidis S., Magorrian J., Moore B., 2004, ApJ, 601, 37
Kereš D., Katz N., Fardal M., Davé R., Weinberg D. H., 2009, MNRAS, 395, 160
Kereš D., Katz N., Weinberg D. H., Davé R., 2005, MNRAS, 363, 2
Khochfar S., Silk J., 2006, ApJ, 648, L21
Kormendy J., 1977, ApJ, 218, 333
Lackner C. N., Cen R., Ostriker J. P., Joung M. R., 2012, arXiv:1206.0295
Lackner C. N., Gunn J. E., 2012, MNRAS, p. 2423
Lackner C. N., Ostriker J. P., 2010, ApJ, 712, 88
Laporte C. F. P., White S. D. M., Naab T., Ruszkowski M., Springel V., 2012, arXiv:1202.2357
Longhetti M., Saracco P., Severgnini P., Della Ceca R., Mannucci F., Bender R., Drory N., Feulner G., Hopp U., 2007, MNRAS, 374, 614
Lotz J. M., Jonsson P., Cox T. J., Croton D., Primack J. R., Somerville R. S., Stewart K., 2011, ApJ, 742, 103
Lynden-Bell D., 1967, MNRAS, 136, 101
Martinez-Manso J., Guzman R., Barro G., Cenarro J., Perez-Gonzalez P., Sanchez-Blazquez P., Trujillo I., Balcells M., Cardiel N., Gallego J., Hempel A., Prieto M., 2011, ApJ, 738, L22
McLure R. J., Pearce H. J., Dunlop J. S., Cirasuolo M., Curtis-Lake E., Bruce V. A., Caputi K., Almaini O., Bonfield D. G., Bradshaw E. J., Buitrago F., Chuter R., Foucaud S., Hartley W. G., Jarvis M. J., 2012, arXiv:1205.4058
Merritt D., 1996, AJ, 111, 2462
Miller R. H., Smith B. F., 1980, ApJ, 235, 421
Misgeld I., Hilker M., 2011, MNRAS, 414, 3699
Moster B. P., Naab T., White S. D. M., 2012, arXiv:1205.5807
Naab T., Johansson P. H., Ostriker J. P., 2009, ApJ, 699, L178
Naab T., Johansson P. H., Ostriker J. P., Efstathiou G., 2007, ApJ, 658, 710
Naab T., Khochfar S., Burkert A., 2006, ApJ, 636, L81
Naab T., Trujillo I., 2006, MNRAS, 369, 625
Nakamura T. K., 2000, ApJ, 531, 739
Navarro J. F., Frenk C. S., White S. D. M., 1997, ApJ, 490, 493
Nelson A. F., Wetzstein M., Naab T., 2009, ApJS, 184, 326
Newman A. B., Ellis R. S., Bundy K., Treu T., 2012, ApJ, 746, 162
Newman A. B., Ellis R. S., Treu T., Bundy K., 2010, ApJ, 717, L103
Nipoti C., Londrillo P., Ciotti L., 2003, MNRAS, 342, 501
Nipoti C., Treu T., Auger M. W., Bolton A. S., 2009, ApJ, 706, L86
Nipoti C., Treu T., Bolton A. S., 2009, ApJ, 703, 1531
Nipoti C., Treu T., Leauthaud A., Bundy K., Newman A. B., Auger M. W., 2012, ArXiv e-prints

Oser L., Naab T., Ostriker J. P., Johansson P. H., 2012, ApJ, 744, 63
Oser L., Ostriker J. P., Naab T., Johansson P. H., Burkert A., 2010, ApJ, 725, 2312
Prugniel P., Simien F., 1997, A&A, 321, 111
Raichoor A., Mei S., Stanford S. A., Holden B. P., Nakata F., Rosati P., Shankar F., Tanaka M., Ford H., Huertas-Company M., Illingworth G., Kodama T., Postman M., Rettura A., Blakeslee J. P., Demarco R., Jee M. J., White R. L., 2012, ApJ, 745, 130
Saracco P., Longhetti M., Andreon S., 2009, MNRAS, 392, 718
Shu F. H., 1978, ApJ, 225, 83
Spergel D. N., Hernquist L., 1992, ApJ, 397, L75
Szomoru D., Franx M., van Dokkum P. G., 2011, arXiv:1111.3361
Szomoru D., Franx M., van Dokkum P. G., 2012, ApJ, 749, 121
Taylor E. N., Franx M., Glazebrook K., Brinchmann J., van der Wel A., van Dokkum P. G., 2010, ApJ, 720, 723
Thomas J., Saglia R. P., Bender R., Thomas D., Gebhardt K., Magorrian J., Corsini E. M., Wegner G., Seitz S., 2011, MNRAS, 415, 545
Toft S., Gallazzi A., Zirm A., Wold M., Zibetti S., Grillo C., Man A., 2012, ArXiv e-prints
Toft S., van Dokkum P., Franx M., Labbe I., Förster Schreiber N. M., Wuyts S., Webb T., Rudnick G., Zirm A., Kriek M., van der Werf P., Blakeslee J. P., Illingworth G., Rix H.-W., Papovich C., Moorwood A., 2007, ApJ, 671, 285
Tremaine S., Richstone D. O., Byun Y., Dressler A., Faber S. M., Grillmair C., Kormendy J., Lauer T. R., 1994, AJ, 107, 634
Trujillo I., Carrasco E. R., Ferré-Mateu A., 2012, ApJ, 751, 45
Trujillo I., Cenarro A. J., de Lorenzo-Cáceres A., Vazdekis A., de la Rosa I. G., Cava A., 2009, ApJ, 692, L118
Trujillo I., Conselice C. J., Bundy K., Cooper M. C., Eisenhardt P., Ellis R. S., 2007, MNRAS, 382, 109
Trujillo I., Ferreras I., de la Rosa I. G., 2011, arXiv:1102.3398
Trujillo I., Ferreras I., de La Rosa I. G., 2011, MNRAS, 415, 3903
Trujillo I., Förster Schreiber N. M., Rudnick G., Barden M., Franx M., Rix H.-W., Caldwell J. A. R., McIntosh D. H., Toft S., Häussler B., Zirm A., van Dokkum P. G., Labbé I., 2006, ApJ, 650, 18
Valentinuzzi T., Poggianti B. M., Saglia R. P., Aragón-Salamanca A., Simard L., Sánchez-Blázquez P., D'onofrio M., Cava A., Couch W. J., Fritz J., Moretti A., Vulcani B., 2010, ApJ, 721, L19
van de Sande J., Kriek M., Franx M., van Dokkum P. G., Bezanson R., Whitaker K. E., Brammer G., Labbé I., Groot P. J., Kaper L., 2011a, arXiv:1104.3860
van de Sande J., Kriek M., Franx M., van Dokkum P. G., Bezanson R., Whitaker K. E., Brammer G., Labbé I., Groot P. J., Kaper L., 2011b, ApJ, 736, L9
van der Wel A., Franx M., van Dokkum P. G., Rix H.-W., Illingworth G. D., Rosati P., 2005, ApJ, 631, 145
van der Wel A., Holden B. P., Zirm A. W., Franx M., Rettura A., Illingworth G. D., Ford H. C., 2008, ApJ, 688, 48
van Dokkum P., Conroy C., 2012, arXiv:1205.6471
van Dokkum P. G., Conroy C., 2010, Nature, 468, 940
van Dokkum P. G., Franx M., Kriek M., Holden B., Illingworth G. D., Magee D., Bouwens R., Marchesini D., Quadri R., Rudnick G., Taylor E. N., Toft S., 2008, ApJ, 677, L5
van Dokkum P. G., Kriek M., Franx M., 2009, Nature, 460, 717
van Dokkum P. G., Whitaker K. E., Brammer G., Franx M., Kriek M., Labbé I., Marchesini D., Quadri R., Bezanson R., Illingworth G. D., Muzzin A., Rudnick G., Tal T., Wake D., 2010, ApJ, 709, 1018
Villumsen J. V., 1983, MNRAS, 204, 219
Wetzstein M., Nelson A. F., Naab T., Burkert A., 2009, ApJS, 184, 298
White S. D. M., 1978, MNRAS, 184, 185
White S. D. M., 1979, MNRAS, 189, 831
White S. D. M., 1980, MNRAS, 191, 1P
White S. D. M., Narayan R., 1987, MNRAS, 229, 103
Williams R. J., Quadri R. F., Franx M., 2011, ApJ, 738, L25
Williams R. J., Quadri R. F., Franx M., van Dokkum P., Toft S., Kriek M., Labbé I., 2010, ApJ, 713, 738
Wuyts S., Cox T. J., Hayward C. C., Franx M., Hernquist L., Hopkins P. F., Jonsson P., van Dokkum P. G., 2010, ApJ, 722, 1666
Zirm A. W., van der Wel A., Franx M., Labbé I., Trujillo I., van Dokkum P., Toft S., Daddi E., Rudnick G., Rix H., Röttgering H. J. A., van der Werf P., 2007, ApJ, 656, 66